metals

MDPI

Article

A Comparative Investigation of Duplex and Super Duplex Stainless Steels Processed through Laser Powder Bed Fusion

Leonidas Gargalis [1], Leonidas Karavias [1], Joachim S. Graff [2], Spyros Diplas [2], Elias P. Koumoulos [3] and Evangelia K. Karaxi [1,*]

[1] Conify, Lavrion Ave.1, Lavrion Technological and Cultural Park (LTCP), 19500 Lavrion, Greece
[2] SINTEF Industry, Forskningsveien 1, 0373 Oslo, Norway
[3] IRES—Innovation in Research & Engineering Solutions, Rue Koningin Astritlaan 59B, 1780 Wemmel, Belgium
* Correspondence: ekaraxi@conify.gr

Abstract: The aim of this paper was to compare duplex (DSS) and super duplex stainless steel processed by laser powder bed fusion (LPBF) based on the process parameters and microstructure–nanomechanical property relationships. Each alloy was investigated with respect to its feedstock powder characteristics. Optimum process parameters including scanning speed, laser power, beam diameter, laser energy density, and layer thickness were defined for each alloy, and near-fully dense parts (>99.9%) were produced. Microstructural analysis was performed via optical (OM), scanning electron microscopy (SEM) and electron backscatter diffraction (EBSD). The samples were subjected to stress relief and high-temperature annealing. EBSD revealed the crystallographic orientation and quantified the phases in the as-built and annealed sample conditions. The as-built samples revealed a fully ferritic microstructure with a small amount of grain boundary austenite in the SDSS microstructure. High-temperature solution annealing resulted in the desired duplex microstructure for both alloys. There were no secondary phases present in the microstructure after both heat treatments. Nanoindentation generated nanomechanical (modulus) mapping grids and quantified the nanomechanical (both hardness and modulus) response; plasticity and stress relief were also assessed in all three conditions (as-built, stress-relieved, and annealed) in both DSS and SDSS. Austenite formation in the annealed condition contributed to lower hardness levels (~4.3–4.8 Gpa) and higher plastic deformation compared to the as-built (~5.7–6.3 Gpa) and stress-relieved conditions (~4.8–5.8 Gpa) for both alloys. SDSS featured a ~60% austenite volume fraction in its annealed and quenched microstructure, attributed to its higher nickel and nitrogen contents compared to DSS, which exhibited a ~30% austenite volume fraction.

Keywords: duplex stainless steel; super duplex stainless steel; electron backscatter diffraction; nanoindentation; laser powder bed fusion; additive manufacturing; ferrite; austenite

Citation: Gargalis, L.; Karavias, L.; Graff, J.S.; Diplas, S.; Koumoulos, E.P.; Karaxi, E.K. A Comparative Investigation of Duplex and Super Duplex Stainless Steels Processed through Laser Powder Bed Fusion. *Metals* **2023**, *13*, 1897. https://doi.org/10.3390/met13111897

Academic Editor: Antonio Mateo

Received: 30 September 2023
Revised: 3 November 2023
Accepted: 11 November 2023
Published: 16 November 2023
Corrected: 20 March 2024

1. Introduction

Duplex stainless steels are iron–nickel–chromium alloys with a characteristic ferritic–austenitic microstructure at ambient temperatures. These alloys inherently offer advantageous mixing of the austenitic and ferritic phases. In comparison to ferritic stainless steel, duplex stainless steels demonstrate enhanced toughness and improved weldability, while they exhibit elevated strength and enhanced corrosion resistance when compared to austenitic stainless steel [1]. Their excellent engineering performance has driven their expanded utility across diverse applications, predominantly within corrosive surroundings like sour gas pipelines and chemical reaction vessels [2,3]. Recently, duplex stainless steel was also used for biomedical applications [4,5]. The most common grades of duplex stainless steel encompass DSS 2205, also known as UNS S31803 (with a composition of 22% Cr, 3% Mo, 5% Ni, and 0.15% N), and SDSS 2507, or UNS S32750 (comprising 25% Cr, 4% Mo, 7% Ni, and 0.25% N) [6,7]. Super duplex stainless steel (SDSS) contains higher contents of

nitrogen (N) and molybdenum (Mo), leading to higher corrosion resistance, strength, and structural stability in comparison to DSS [8].

Given the challenges linked to machining and shaping duplex stainless steels, and recognizing the limitations of powder metallurgy free-form fabrication, such as the tendency to yield porous structures, utilizing laser powder bed fusion (LPBF) as an additive manufacturing (AM) technology for duplex stainless steels has become a potential state of the art in manufacturing [9]. Wire arc additive manufacturing (WAAM) [10,11], laser-directed energy deposition (L-DED) [12], and laser powder bed fusion (LPBF) represent the dominant metal AM methods for the production of DSS and SDSS parts [13].

LPBF-produced components have unique microstructures due to high-temperature gradients and rapid solidification in the melt pool. These result in an epitaxial-to-columnar grain structure aligned with the build direction. The morphology, crystallography, and average grain size vary significantly with changes in process parameters and laser scanning. LPBF's ability to create fine grains and substructures enhances mechanical properties compared to traditionally manufactured wrought and cast parts [14,15].

Studies can be found in the literature where the process optimization of commercially available duplex and super duplex stainless steel powders is presented [16,17]. In some studies, the focus is on the analysis of the microstructure and the impact on mechanical properties [18–20], and in others, research is performed to quantify phases and their effect on corrosion resistance [21,22]. Different methodologies for the parameter optimization of DSS and SDSS LPBF processing were based on experiments exploring a wide range of the processing parameters combined with statistical analyses, or on thermodynamic calculations studying the formation of embrittling phases upon laser processing or post-AM heat treatment [9,15–18,20,22]. Other studies correlated microstructure evolution and second-phase precipitation with mechanical properties (ultimate tensile strength, elongation at break, microhardness) and/or corrosion behavior [15,20,23,24]. In other studies, the authors developed new alloys, suitable for LPBF, by the dry mixing of elemental powders and/or pre-alloyed powders, allowing them to create custom duplex and super duplex powder blends with tailored chemical compositions. The aim was to promote austenite formation in the as-built condition [25–27].

In equilibrium conditions (low cooling rates), duplex stainless steels are solidified according to ferritic–austenitic solidification, where the ferrite solidifies first followed by austenite formation [28,29]. When non-equilibrium conditions (high cooling rates up to 10^5–10^6 °C/s for LPBF) prevail [30], ferrite dominates the microstructure since the solidification mode alters from ferrite–austenite (FA) to only ferrite (F) [31]. Thus, the duplex and super duplex stainless steel microstructure is mainly ferritic as reported in numerous LPBF-related studies [16,20,32–34]. Given the prevalence of ferrite in the LPBF as-built microstructure, an excess of nitrogen (N) saturation within the ferrite matrix has been reported to induce the formation of chromium nitride precipitates [15,20]. Secondary phases (sigma, chi), chromium nitrides, and carbides comprise the most common precipitations of duplex stainless steels when they are subjected to temperatures ranging from 600 °C to 1000 °C [35]. However, during the LPBF process, extremely high cooling rates inhibit the formation of sigma and chi phases. Nano-secondary phases (α′, G) usually precipitate under 600 °C and specifically within the temperature range of 300 °C to 550 °C after prolonged heat exposure [36,37]. Thus, in various studies, the authors used solution annealing at high temperatures (>1000 °C) as a post processing step. These studies showed an Increase in the austenite content in the microstructure, producing a phase balance between austenite and ferrite while avoiding the precipitation of secondary phases and dissolution of chromium nitrides, which are deleterious for mechanical/anti-corrosion properties [15,20,33,34]. With respect to the microstructural constituents, in duplex stainless steels, the ratio between austenite and ferrite phases significantly governs the properties related to strength and corrosion resistance [38,39]. The critical phase balance between phases within DSS and SDSS can be disrupted due to alterations in composition and thermal effects associated with cooling rates during fabrication [32].

After annealing and subsequent quenching, the ductility is restored with the formation of austenite and microstructure reallocation, while hardness, yield, and tensile strength are reduced [15,33,34]. More specifically, the reported findings concerning the mechanical properties of the constituent phases (ferrite and austenite) of conventionally manufactured DSS/SDSS at the nanoscale display considerable variation [40–42]. The hardness and elastic modulus of the austenitic phase can differ—being higher, lower, or on par with those of the ferritic phase. These variations hinge on diverse factors such as the processing approach under scrutiny.

In the absence of a comparative study between duplex and super duplex stainless steels, the current investigation sought to assess DSS (2205) and SDSS (2507) for their printability via LPBF technology. The comparison between these alloys was focused on microstructural investigations via relevant microscopy and diffraction techniques. Based on the existing literature and industrial standards, common heat treatment procedures for DSS and SDSS were selected to assess their impact on microstructure evolution, namely stress relief and solution annealing followed by water quenching. In addition, nanoindentation tests were carried out to measure the nanomechanical properties in all three conditions (as-built, stress-relieved, and annealed), and the results were effectively correlated with their respective microstructures. The objective of this study was to facilitate comprehensive comparisons between the two alloys in the as-built and heat-treated conditions, observe their nanomechanical response, and link these to their microstructure constituents and the chemical composition of the powder feedstock.

2. Materials and Methods

2.1. Feedstock Materials

Gas-atomized duplex stainless steel grade 2205 (1.4462) (MARS F51, Mimete S.r.l., Biassono, Italy) and super duplex stainless steel 2507 (1.4410) (MARS F53, Mimete S.r.l., Biassono, Italy) metal powders were used as feedstock. Their chemical compositions are illustrated in Table 1. Both metal powders were extensively studied in terms of their powder characteristics (apparent density, tap density, flowability, particle shape and morphology, and D10, D50, and D90 values) and chemical composition. A small quantity of metal powder was collected according to the procedures recommended under ASTM B215-20. Tap and apparent density were measured according to the ASTM B527-22 and ASTM B212-21 standards, correspondingly. Flowability was tested according to the ASTM B213-20 standard. D10, D50, and D90 values and the equivalent circle diameter (ECD) were measured with static image analysis through Morphologi 4 (Malvern Panalytical Ltd., Malvern, UK) according to the ISO 13322-1:2014 standard [43]. The chemical composition of the powders was analyzed via electron dispersive spectroscopy (EDS) with 0.1% accuracy integrated to a Phenom ProX (Thermo Fisher Scientific Inc., Waltham, MA, USA) scanning electron microscope (SEM). Furthermore, powders of both alloys were mounted, ground, and polished in order to assess internal porosity via SEM analysis.

Table 1. Chemical composition of the as-received feedstock powder materials in weight %.

Duplex Stainless Steel 2205										
C	**S**	**N**	**Cr**	**Fe**	**Mn**	**Mo**	**Ni**	**P**	**Si**	**Cu**
0.022	0.005	0.13	22.1	Bal.	1.03	3.2	5.2	0.01	0.51	-
Super Duplex Stainless Steel 2507										
0.013	0.005	0.29	24.7	Bal.	0.77	3.6	8.0	0.011	0.45	0.01

2.2. LPBF Parameter Optimization and Post-AM Heat Treatment

Processing of metallic powders was carried out using an LPBF machine (INTECH, SF1 iFusion150, Intech Additive Solutions Ltd., Bangalore, India), which features a 500 W ytterbium-fiber laser operating at 1064 nm with an 80 µm laser spot size. The samples were

built on a 150 mm-diameter platform composed of AISI 304 stainless steel. Throughout the manufacturing process, the build plate was preheated and consistently maintained at a temperature of 150 °C. The build chamber was maintained under an inert atmosphere using high-purity argon gas (Grade 5.0) whilst oxygen levels were carefully controlled to remain below 0.5 ppm. Data preparation was carried out using the AMBuilder software developed by INTECH (Intech Additive Solutions Ltd., Bangalore, India). Initial experimental trials were conducted using 2205 duplex and 2507 super duplex stainless steels, with variations in laser power, scan speed, and hatch distance to establish a narrow range of suitable process parameters. To determine the optimal set of process parameters, the volumetric energy density (VED) was calculated using Equation (1):

$$E = \frac{P}{v \cdot h \cdot t} (\mathrm{J/mm^3}) \quad (1)$$

where P is the laser power in W, v is the laser scan speed in mm/s, h is the hatch distance between adjacent laser scan tracks in mm, and t is the layer thickness of the powder in mm. The resulting optimum VED for both alloys was found in the range falling within 59–65 J/mm^3. It is important to highlight that the variations in energy densities were attributed to changes in laser power, scan speed, and hatching distance, as detailed in Tables 2 and 3 for DSS and SDSS, respectively. The layer thickness remained consistent at 40 µm, and the hatch distance varied between 100 and 120 µm. To facilitate easy removal from the substrate, cylindrical samples were manufactured with a diameter of 12.5 mm and a height of 8 mm, utilizing 3 mm support structures. The samples were removed from the substrate by cutting the supports with a bandsaw machine (FEMI N310 DA DG, Castel Guelfo di Bologna, Italy). The experimental plan was divided into 2 builds per alloy comprising different samples on the substrates, and their respective VED is shown in Figure 1. Heat treatments of the optimum as-built samples were conducted in a high-temperature electrical furnace (THERMANSYS BOX-AS20–1600, Thessaloniki, Greece) under atmospheric conditions as described below: (1) stress relief annealing at 300 °C for 4 h to minimize/eliminate residual stresses and (2); solution annealing at 1100 °C for 1 h followed by water quenching to restore the duplex microstructure by the nucleation and growth of austenite without secondary-phase precipitation [38–40].

Table 2. DOE and process parameter window for DSS (2205).

No. of Sample	Laser Power (W)	Scan Speed (mm/s)	Hatch Distance (µm)	Laser Beam Spot Size (µm)	Layer Thickness (µm)	Volumetric Energy Density (J/mm^3)
1	113	357	120	80	40	65.94
2	204	769	100	80	40	66.32
3	226	940	110	80	40	54.64
4	269	1058	100	80	40	63.56
5	296	1130	100	80	40	65.49
6	304	946	110	80	40	73.03
7	317	1189	100	80	40	66.65
8	334	963	120	80	40	72.25
9	347	1242	100	80	40	69.84
10	363	1056	120	80	40	71.61
11	425	1329	110	80	40	72.68
12	467	1346	120	80	40	72.28

Table 3. DOE and process parameter window for SDSS (2507).

No. of Sample	Laser Power (W)	Scan Speed (mm/s)	Hatch Distance (μm)	Laser Beam Spot Size (μm)	Layer Thickness (μm)	Volumetric Energy Density (J/mm^3)
1	95	331	120	80	40	59.79
2	125	408	110	80	40	69.63
3	169	590	120	80	40	59.67
4	182	723	100	80	40	62.93
5	187	566	100	80	40	82.59
6	189	781	120	80	40	50.41
7	192	661	120	80	40	60.51
8	262	794	110	80	40	74.99
9	267	894	110	80	40	67.87
10	305	1174	110	80	40	59.04
11	336	1230	100	80	40	68.29
12	347	1016	110	80	40	77.62

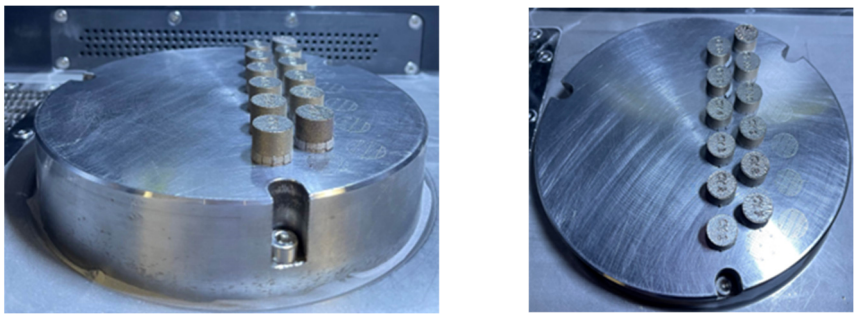

(**a**) (**b**)

Figure 1. Images of (**a**) DSS (2205) and (**b**) SDSS (2507) samples for parameter optimization, prior to removal from the substrate.

2.3. Density and Microstructure of LPBF-Processed As-Built and Heat-Treated Samples

Metallographic preparation was performed on all as-built samples, including cutting using a micro-cutting machine (Mecatome T210, precision micro-cutting machine, PRESI, Paris, France), mounting, grinding, and polishing using the Tegramin system (STRUERS, Birmensdorf, Switzerland). This preparation aimed to evaluate and quantify defects like cracks or pores in the samples. The specimens were sequentially grounded with coarser grades up to a 2000-grit finish, followed by polishing using a 3 μm diamond paste and finally a 1 μm polishing. After polishing, two different chemical solutions were utilized for the etching of as-built and heat-treated samples. The as-built and stress-relieved samples were chemically etched with Beraha's etchant (100 mL H_2O + 20 mL HCL + 1 gr Potassium Metabisulfite) to unveil the microstructure and obtain the optimal phase differentiation between austenite and ferrite. The etching duration ranged from 5 to 20 s considering the freshness of the etching solution and mostly in the time interval between the last polishing step and etching. Beraha's etchant selectively darkens the ferrite phase while leaving the austenite phase unaffected and bright in duplex stainless steels [44]. The annealed samples were electrolytically etched with sodium hydroxide solution (NaOH, 20% w/v) and an applied voltage of 5 V for 10 s. NaOH solution proved to be a better choice than Beraha for the annealed samples, especially for SEM microstructure observations. The density of the printed samples as well as the phase quantification of ferrite/austenite in the annealed and water-quenched microstructures was determined using ImageJ (1.54 d, NIH and LOCI, Madison, WI, USA). The average density values were calculated for each sample by analyzing optical micrographs captured in XY and XZ planes (5 micrographs per plane, i.e., 10 micrographs per sample). The phase quantification in the annealed and water-quenched microstructures was conducted on SEM micrographs due to their

higher image quality favored for thresholding (average of 5 micrographs per sample). The micrographs were selected from the bottom, the middle, and the top side of the XZ plane for each sample in order to have a representative number of measurements. The characterization and quantification of phases was validated through EBSD.

OM was employed to capture images of the sample's overall microstructure, at magnifications ranging from 50X to 500X using a 40–800X Trinocular Metallurgical Polarization Microscope equipped with an 18 MP Digital Camera from AMScope (United Scope LLC., Irvine, CA, USA). For higher magnification imaging, SEM was utilized to capture images with magnifications up to 150,000X. The sample microstructures were analyzed with the same SEM as the one utilized in 2.1, using an acceleration voltage of 15 KeV, in combination with EDS for compositional analysis.

EBSD was conducted on an FEI Nova NanoSEM 650 scanning electron microscope (FEI, Brno, Czech Republic) with a TSL EBSD camera to gain knowledge of how the ferritic and austenitic phase fractions were formed and arranged in the additively manufactured samples. Grain size measurements and fraction quantification of austenite and ferrite phases were also conducted. The analysis was conducted using an electron beam acceleration voltage of 20 keV and a working distance of 20 mm with a step size of 1 μm for the as-built samples and 0.5 μm for the annealed and quenched samples, a binning factor of 4×4, and an exposure time of about 12 ms. The analysis of the EBSD results was conducted by using the Aztec software (version 3.3, Oxford Instruments, PLC, Abingdon, Oxfordshire, UK). The HKL Channel 5 software (Oxford Instruments, Oxford, UK) was also utilized for grain size analysis. The grain sizes of the austenite grains were calculated excluding grains at the edges of the investigated area. The ferrite grains were, in some cases, intermittent by austenite grains and were not continuous. In other cases, the ferrite grains were made up of several sub-grains with minor differences in orientations. Both of these characteristics made it difficult to detect the number of ferrite grains automatically; therefore, they were counted manually. Their total area was calculated from the phase ratio multiplied by the area investigated. Finally, the average area of a grain was calculated and converted to the diameter of a circle, also known as the equivalent circle diameter (ECD). The 0.5 μm step size for the annealed and quenched samples was selected to capture the smaller austenite grains. Thus, the examined area was also reduced. For EBSD analysis, the same metallographic preparation was used. An additional polishing step was applied using a colloidal silica suspension (0.04 μm) to remove scratches after grinding and polishing steps and achieve a pristine surface conducive for high-quality EBSD data.

2.4. Nanoindentation Testing of LPBF-Processed As-Built and Heat-Treated Samples

A Bruker TS77 TriboLab® Nanomechanical Test Instrument (Minneapolis, MN, USA) was employed for the nanoindentation testing (the instrument capabilities enable loading from 1×10^{-3} mN to 30 mN and with a high load and displacement resolution of 1 nN and 0.04 nm, respectively). The instrument is equipped with a scanning probe microscope, in which a probe tip moves in a scan pattern across the sample surface using a three-axis piezo positioner. In this study, a Berkovich tip with a radius of 80 nm was selected. Nanomechanical properties were assessed using the Oliver–Pharr model [45]. A grid-mapping protocol of a 20-by-20-point array was selected, with 10-micron spacing, employing 40 s loading, 3 s hold time, and 40 s unloading time under displacement control (set at 200 nm of displacement). The load range was carefully selected according to [46] where values of reduced modulus were stable within the 3000–7000 μN range. At first, contour maps were generated in order to reproduce the surface topographical variation of local mechanical properties, due to distinct phase occurrence. Within the maps, recurrent patterns were identified and correlated with SEM images of the grid (nanoindented samples were subjected to SEM analysis after the measurements).

3. Results

3.1. Powder Characterization

The SEM micrographs in Figure 2 illustrate the morphology of both feedstock powders and their respective chemical compositions as revealed through EDS. The chemical composition of EDS analysis is in agreement with the chemical composition provided by the supplier (Table 1). Most of the particles were spherical. However, in each sample, trace amounts of satellites, agglomerations, and elongated particles were observed.

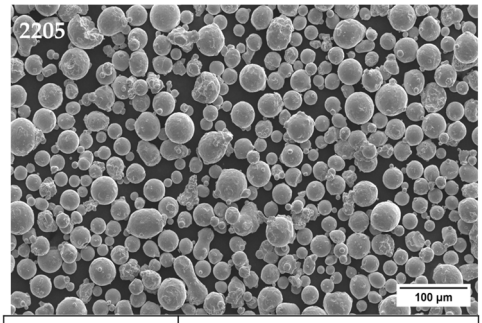

Element	Weight Conc. (%)
Si	0.5
Cr	23.5
Mn	1.6
Fe	65.3
Ni	5.1
Mo	4.0

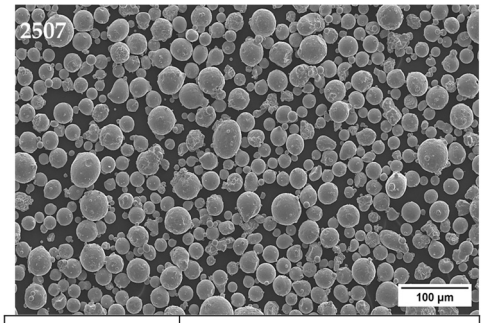

Element	Weight Conc. (%)
Si	0.4
Cr	26.1
Mn	1.4
Fe	61.3
Ni	6.7
Mo	4.1

Figure 2. SEM micrographs of DSS 2205 and SDSS 2507 powders with their respective EDS chemical analysis.

In Figure 3, cross-sections of DSS 2205 and SDSS 2507 powders are illustrated. A very small number of particles featured internal porosity that did not affect the melting behavior or relative density of the final parts [47,48].

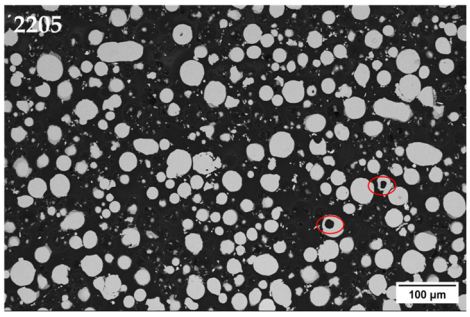

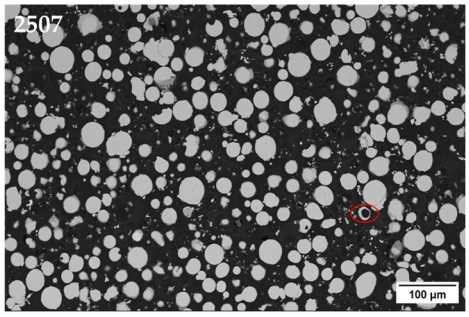

Figure 3. SEM micrographs of polished cross-sections of the feedstock powder materials DSS 2205 and SDSS 2507. Internal porosity in powder particles is indicated by the red circles.

The flowability and apparent and tapped density values of DSS 2205 and SDSS 2507 powders are presented in Table 4, which were almost identical for both powder alloys. The equivalent circle diameter (ECD) for particles of each powder was determined using static image analysis. The minimum, maximum, and mean diameters for each powder were calculated, along with the D10, D50, and D90 values that are presented in Table 5. The cumulative curves of volumetric particle size distribution (Figure 4) were used to obtain the D10, D50, and D90 values for each powder. Both powders exhibited similar values for minimum, maximum, and mean EC diameter. Also, the D10, D50, and D90 values were identical for both powders, indicating a similar width in volume distribution as shown in Figure 4.

Table 4. Duplex stainless steel 2205 and super duplex stainless steel 2507 powder characteristics.

Bulk Powder Characteristics	DSS 2205	SDSS 2507
Apparent density (g/cm^3)	3.9	4.0
Tapped density (g/cm^3)	4.3	4.4
Flowability (s/50 g)	18.9	18.4

Table 5. Powder characteristics obtained through static image analysis.

Particle Size Measurements	DSS 2205	SDSS 2507
Min. Equivalent Circle Diameter (µm)	0.52	0.52
Max. Equivalent Circle Diameter (µm)	84.8	88.2
Equivalent Circle Diameter Mean (µm)	21.5	25.4
Equivalent Circle D10 (µm)	21.9	23.4
Equivalent Circle D50 (µm)	40.4	39.4
Equivalent Circle D90 (µm)	62.5	59.1

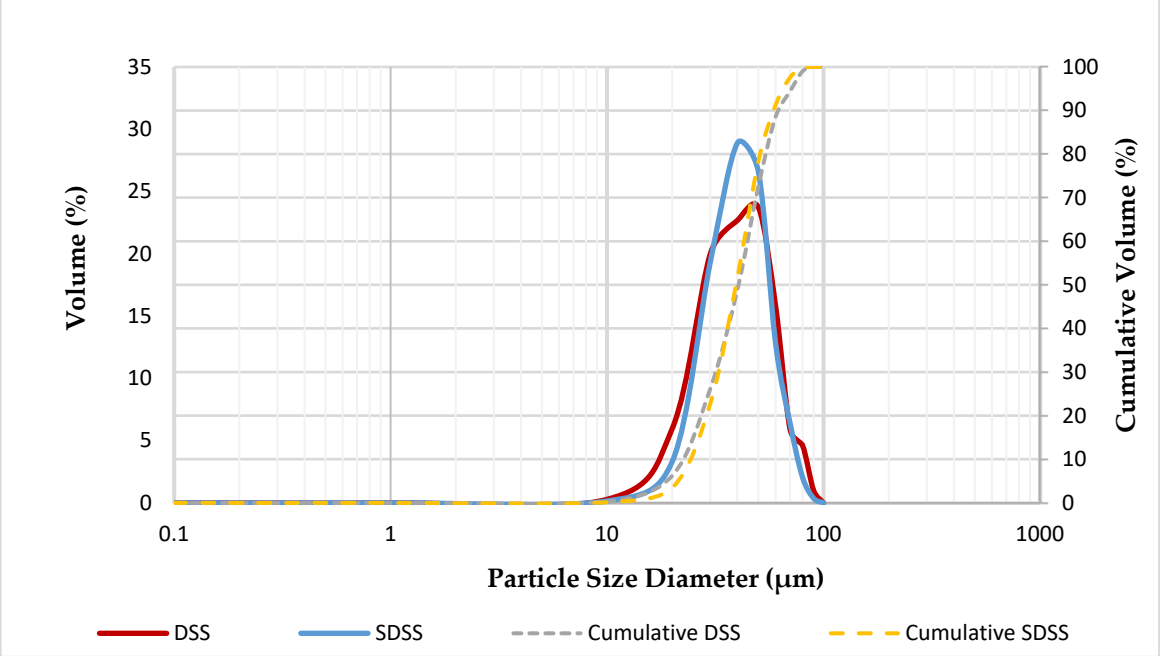

Figure 4. Volumetric EC particle size distribution for DSS 2205 and SDSS 2507.

3.2. Density–Porosity Analysis of LPBF Samples

The sectioned and polished samples revealed that keyhole pores were evident for VED exceeding 80 J/mm^3, whereas a lack-of-fusion porosity was observed mainly for VED values below 55 J/mm^3. The small differences in the chemical composition, and the PSD of the DSS and SDSS feedstock metal powders, can justify minor differences in density and processing regime. It must also be noted that different LPBF machines might use a different optimum processing parameter set to produce near-fully dense samples because there are differences and restrictions imposed by the hardware such as the type of laser, wavelength, laser beam diameter, maximum laser power, etc. [16]. The porosity of the as-built samples with various processing conditions is presented in Figures 5 and 6. It is evident that the porosity is influenced by the volumetric energy input during the LPBF process.

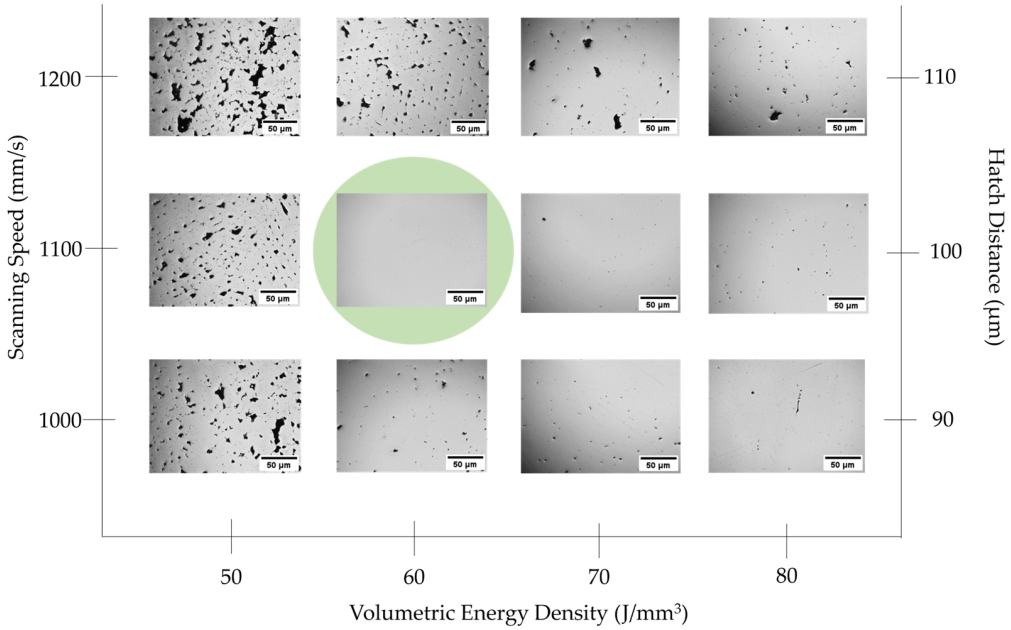

Figure 5. Optical micrographs showing the evolution of porosity in DSS 2205 cylindrical samples built with increasing energy density due to variation of process parameters (scale bar for all micrographs is 50 µm). The green circle indicates the best sample in terms of relative density and the optimum processing parameters.

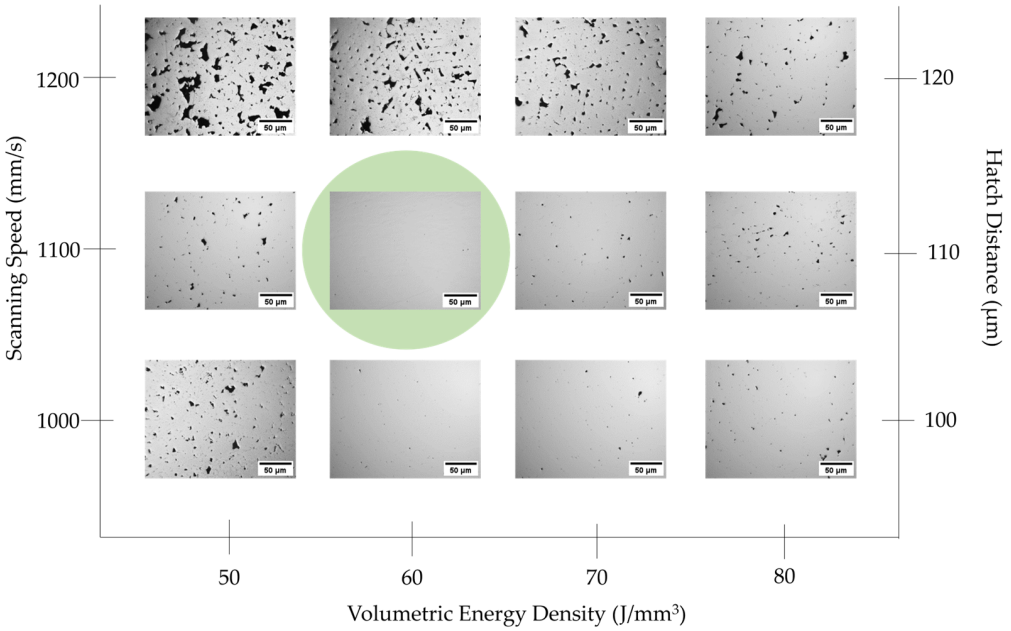

Figure 6. Optical micrographs showing the porosity of SDSS 2507 cylindrical samples built with increasing energy density due to variation of process parameters (scale bar for all micrographs is 50 µm). The green circle indicates the best sample in terms of relative density and the optimum processing parameters.

For duplex (2205) stainless steel, the optimum VED resulted in a relative density of 99.98% in the XY plane and 99.97% in the XZ plane. Similarly for super duplex (2507) stainless steel, the optimum VED resulted in a relative density of 99.95% in the XY plane and 99.96% in the XZ plane, respectively.

Images of cross-sectioned areas of the samples that were subjected to fine polishing were converted to 8-bit grey-scale images, thresholding was applied, and the total surface

area of pores was measured. In Figure 7, optical micrographs with the optimum near-fully dese duplex and super duplex stainless steel samples are presented.

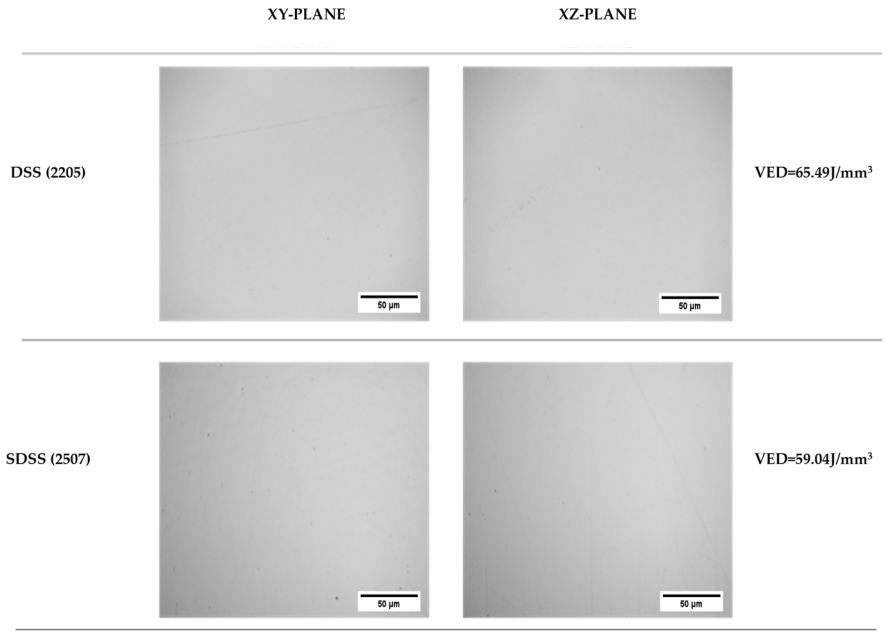

Figure 7. Optical micrographs of near-fully dense duplex (2205) and super duplex (2507) stainless steel samples in the XY and XZ planes, processed with the optimum parameter set for each alloy.

3.3. DSS and SDSS Microstructural Analysis

3.3.1. As-Built DSS 2205

In Figure 8, (a) LOM and (b) SEM micrographs illustrate a fully ferritic microstructure of DSS 2205 with columnar ferrite grains nucleating from both sides of the melt pool and slightly inclined towards the center of the melt pool in the XY plane. In the XZ plane, the columnar ferrite grains nucleate, following the direction of the heat source [49]. Also, melt pool boundaries can be distinguished in the XZ plane, as well as laser melt tracks in the XY plane.

Figures 9 and 10 show the EBSD inverse pole figure (IPF) and phase maps of the as-built DSS sample in the XY and XZ directions, respectively. The "mosaic" structure arising from the selected scanning strategy was evident [50]. EBSD confirmed the fully ferritic microstructure (100%) for both directions (XY and XZ). Austenite traces were also observed, but in <0.1% of the total area of the sample. The fraction of the zero solution was $\leq$0.3% for both directions. Ferrite grains featured a mixed orientation, mostly along the <101> and <111> crystallographic directions. The average grain size corresponded to an equivalent circle diameter of 12.6 µm and 15.9 µm for XY and XZ directions, correspondingly. In the phase map, austenite is shown in blue, ferrite is shown in red, zero solution in white (Figures 9b and 10b), and the scale bar is 200 µm for all micrographs.

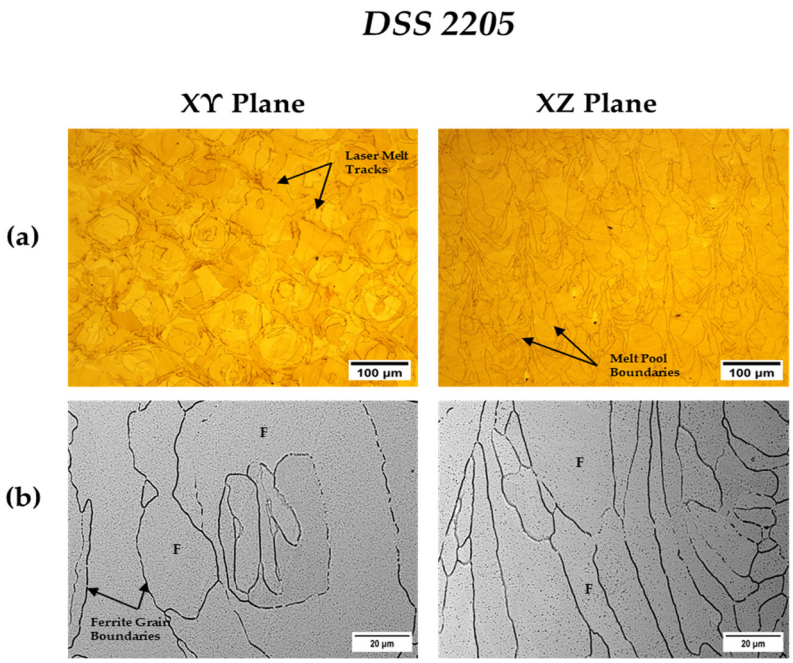

Figure 8. As-built DSS microstructure. (**a**) LOM (light optical microscope) and (**b**) SEM (scanning electron microscope) micrographs transverse to build direction (XY plane) and parallel to build direction (XZ plane). F = ferrite.

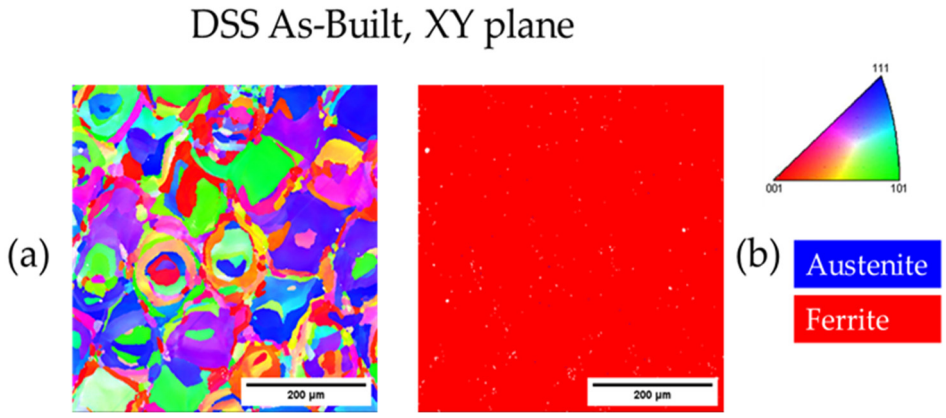

Figure 9. EBSD results of the XY plane in the as-built DSS sample. (**a**) Inverse pole figure map: <001> directions shown in red; <101> directions in green; <111> directions in blue. (**b**) Phase map.

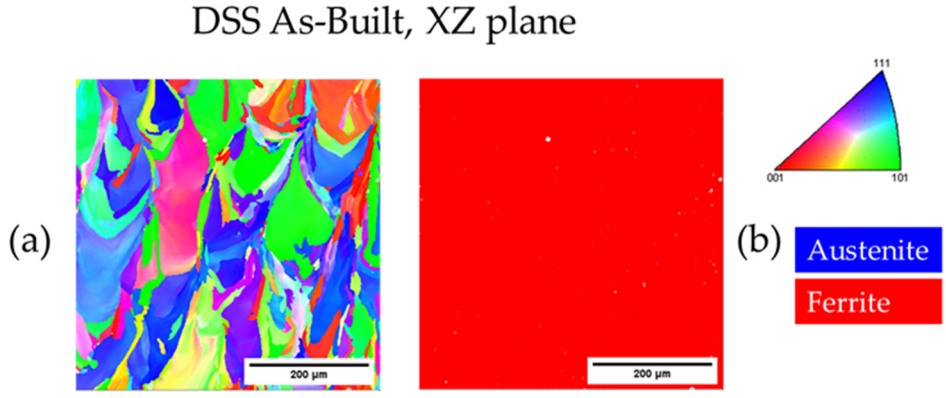

Figure 10. EBSD results of the XZ plane in the as-built DSS sample. (**a**) Inverse pole figure map: <001> directions shown in red; <101> directions in green; <111> directions in blue. (**b**) Phase map.

3.3.2. Heat-Treated DSS 2205

In Figures 11 and 12, the microstructures of stress-relieved DSS and annealed and water-quenched DSS are illustrated, correspondingly. The stress-relieved sample showed the same microstructure as the as-built DSS sample. There was no grain growth or intermetallic phase formation, such as sigma and chi, visible under SEM after the stress relief heat treatment. In the annealed and quenched microstructure, there were tangible changes regarding the austenite volume fraction, grain morphology, and the overall microstructure. In Figure 12, an increased austenite volume fraction can be observed while the solidification structure (melt pool boundaries and laser melt tracks) is not visible in comparison to the as-built DSS microstructure. The austenite in the annealed and water-quenched microstructure exhibited various morphologies, including grain boundary austenite (GBA), intragranular austenite (IGA), and secondary austenite ($\gamma 2$). The EDS analysis aided in the phase identification of different grains by measuring the wt.% of austenite (Ni, Mn) and ferrite-stabilizing elements (Cr, Mo, Si). As expected, austenite exhibited increased Ni (approximately 2 wt.% higher nickel content compared to ferrite) and Mn content, while ferrite showed an approximately 3 wt.% higher chromium content compared to austenite. In Table 6 the EDS results of ferrite and austenite are presented for the annealed/water-quenched DSS sample.

Table 6. EDS analysis results of annealed and water-quenched DSS.

	Elements (wt.%)					
Annealed DSS	**Si**	**Mn**	**Cr**	**Fe**	**Ni**	**Mo**
Ferrite	0.700	-	24.500	66.300	4.100	4.400
Austenite	-	1.205	21.586	68.474	6.225	2.510

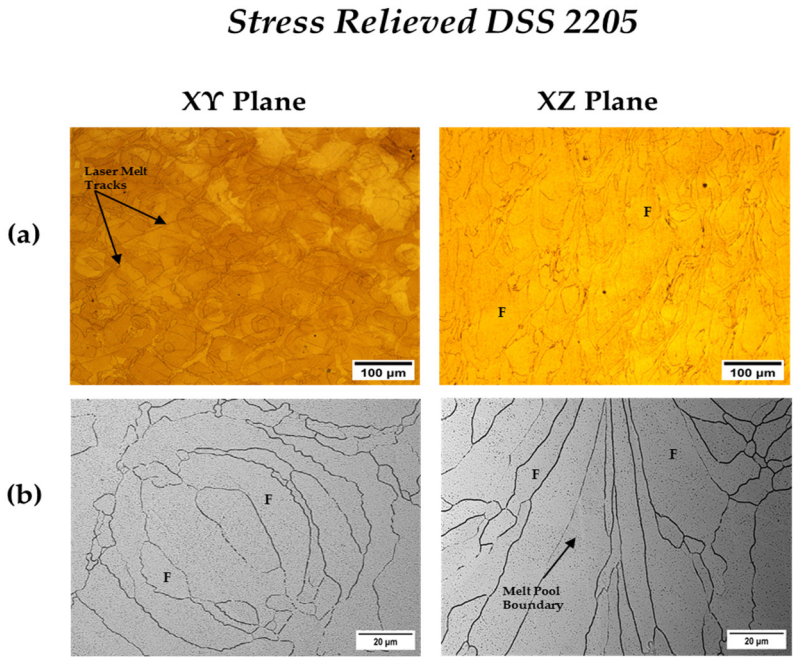

Figure 11. Stress-relieved DSS microstructure. (**a**) LOM (light optical microscope) and (**b**) SEM (scanning electron microscope) micrographs transverse to build direction (XY plane) and parallel to build direction (XZ plane). F = ferrite.

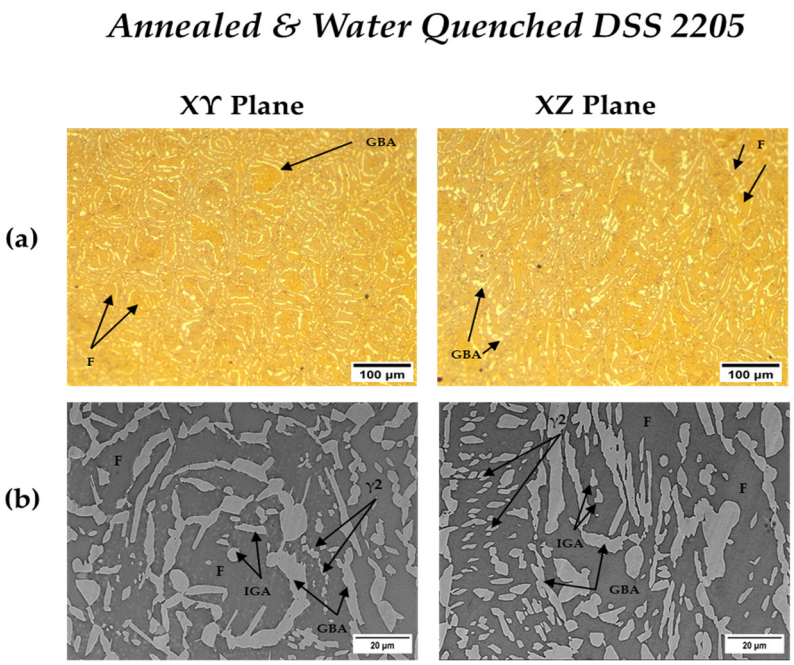

Figure 12. Annealed and water-quenched DSS microstructure. (**a**) LOM (light optical microscope) and (**b**) SEM (scanning electron microscope) micrographs transverse to build direction (XY plane) and parallel to build direction (XZ plane). F = ferrite; GBA = grain boundary austenite; IGA = intragranular austenite; γ2 = secondary austenite.

The increased austenite volume fraction was confirmed and quantified through image analysis. In Figure 13, a representative SEM image before and after thresholding is presented as well as the average of each phase volume fraction for the annealed/water-quenched DSS sample being equal to 34% and 66% for austenite and ferrite, respectively.

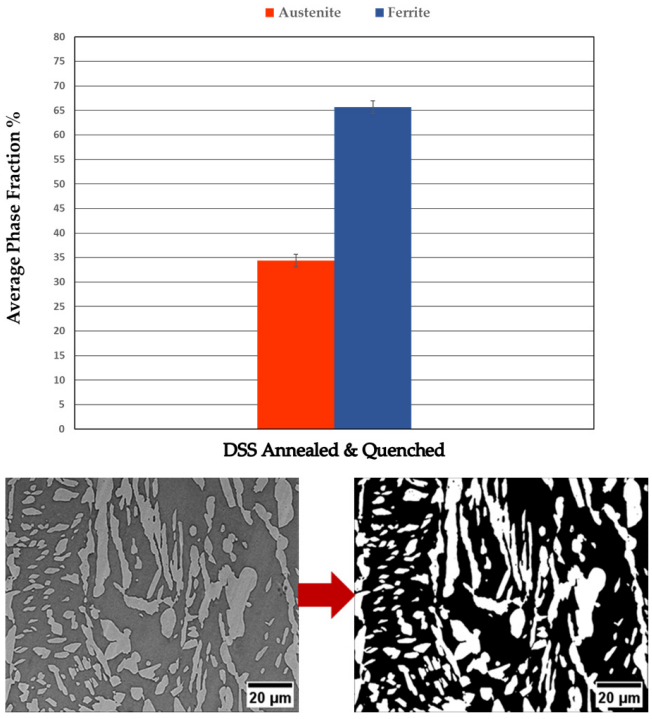

Figure 13. Annealed and water-quenched DSS image analysis results.

Figure 14 shows the EBSD results of the XY plane in the annealed DSS sample. (a) Inverse pole figure map: <001> directions shown in red; <101> directions in green; <111> directions in blue. (b) Phase map. (c) Inverse pole figure map for ferrite only. (d) Inverse pole figure map for austenite only.

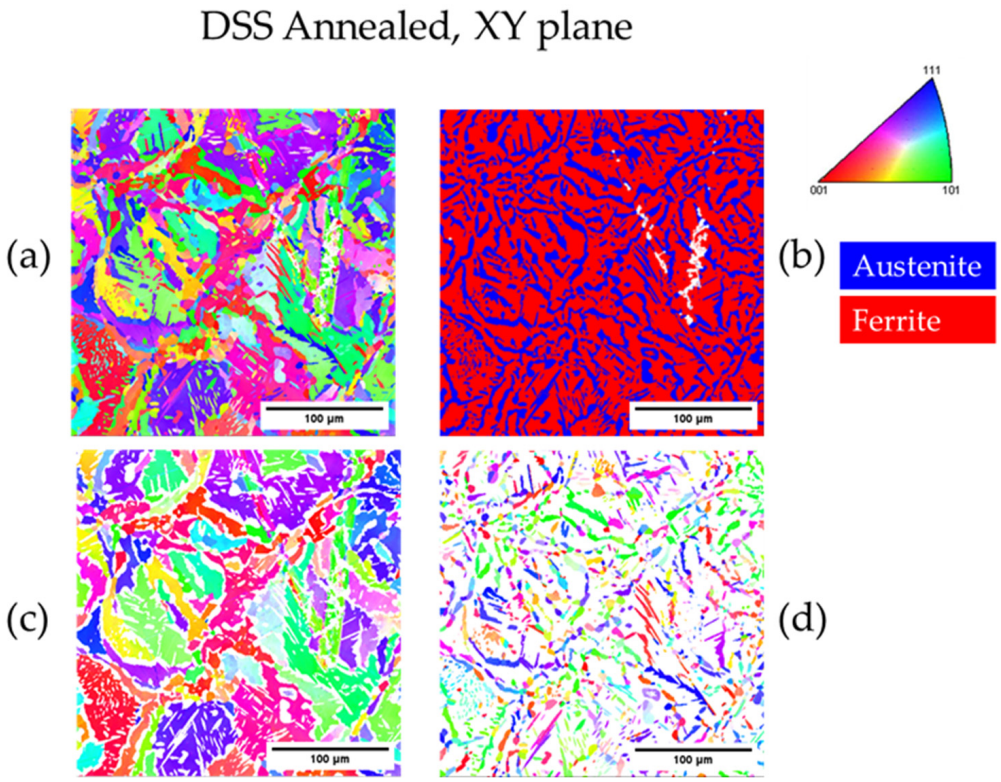

Figure 14. EBSD results of the XY plane in the annealed DSS sample. (**a**) Inverse pole figure map: <001> directions shown in red; <101> directions in green; <111> directions in blue. (**b**) Phase map. (**c**) Inverse pole figure map for ferrite only. (**d**) Inverse pole figure map for austenite only.

In Figure 15, the EBSD IPF and phase maps of the annealed/water-quenched DSS sample in the XY and XZ planes are presented. As also depicted through SEM, the microstructure changed considerably due to the formation of austenite. The "mosaic" structure arising from the selected scanning strategy was still visible, but far less evident. The austenite grains were small and well dispersed. Austenite is shown in blue, ferrite is shown in red, zero solution in white, and the scale bar is 100 µm for all micrographs. The phase fraction of austenite was measured equal to 31.1% and 31.6% in the XY and XZ planes, respectively, which were similar to the values obtained via image analysis.

The fraction of the zero solution was $\leq$1.0% for both directions. Ferrite grains featured a mixed orientation along the <001> and <111> crystallographic directions, mostly for the XY plane, and a strong orientation along the <101> crystallographic direction for the XZ plane. Austenite grains featured a mixed orientation along the <111> and <101> crystallographic directions, mostly for the XY plane, and mixed orientation along the <001>, <111>, and <101> crystallographic directions for the XZ plane. The average grain size corresponded to an equivalent circle diameter of 22 µm and 25 µm for ferrite as seen in the XY and XZ directions, and 3.3 µm and 3.4 µm for austenite, as seen in the XY and XZ directions, respectively.

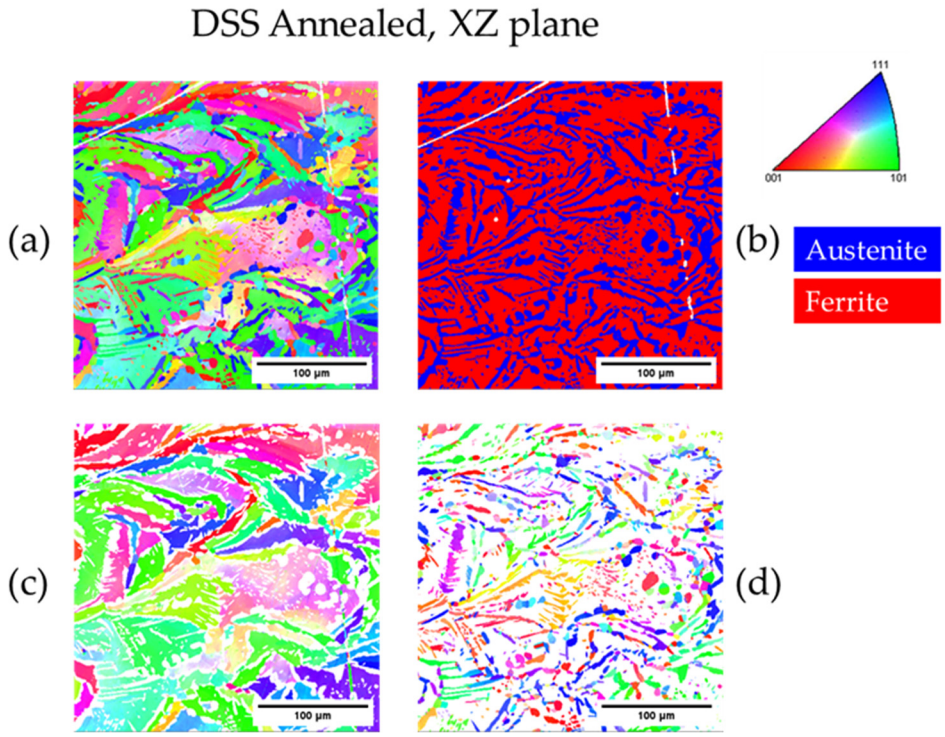

Figure 15. EBSD results of the XZ plane in the annealed DSS sample. (**a**) Inverse pole figure map: <001> directions shown in red; <101> directions in green; <111> directions in blue. (**b**) Phase map. (**c**) Inverse pole figure map for ferrite only. (**d**) Inverse pole figure map for austenite only.

3.3.3. As-Built SDSS 2507

Columnar ferrite grains were observed in the SDSS 2507 microstructure as well as micro-crystalline grain boundary austenite (GBA) (Figure 16). Grain boundary austenite nucleated between the ferrite grains, along the ferrite–ferrite grain boundaries [20]. SEM showed the allotriomorphic shape and morphology of the austenitic phase exhibiting greater grain size near intersections of melt pool boundaries. More specifically, the volume fraction of austenite was higher near the intersections of the melt pool boundaries in the XZ plane and near the overlaps of the laser melt tracks in the XY plane (Figure 16b). Table 7 includes the EDS analysis of the characteristic microstructural constituents. Similar to the DSS case, the weight percentage differences of austenite/ferrite-stabilizing elements was used to identify grain boundary austenite and ferrite. The main difference was detected in Mo concentrations being equal to 7 wt.% for ferrite and 4 wt.% for grain boundary austenite, respectively. Furthermore, in Figure 16b, a Ni-rich micro-segregation was observed as well as sub-micro-grains along the length of melt pool boundaries (XZ plane) and laser melt track boundaries (XY plane). The Ni-rich segregation region was also identified through EDS analysis (23.1 wt.% Ni) (Table 7).

Table 7. EDS analysis results of as-built SDSS.

	Elements (wt.%)					
As-Built SDSS	**Si**	**Mn**	**Cr**	**Fe**	**Ni**	**Mo**
Ferrite	1.7	-	26.4	58.8	6.2	6.9
Grain Boundary Austenite	-	0.9	25.8	62.4	7.0	4.1
Segregation	-	-	23.9	46.7	23.1	6.4

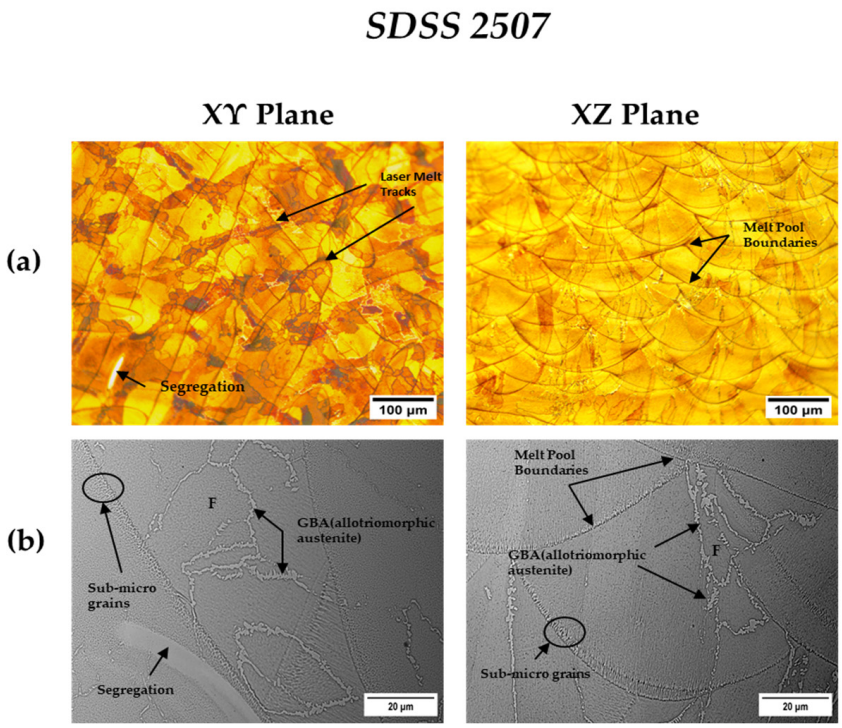

Figure 16. As-built SDSS microstructure. (**a**) LOM and (**b**) SEM micrographs transverse to build direction (XY plane) and parallel to build direction (XZ plane). F = ferrite; GBA = grain boundary austenite.

In Figures 17 and 18 the EBSD IPF and phase maps are presented for the as-built SDSS sample in the XY and XZ planes, respectively. There were many similarities with the as-built DSS samples. The "mosaic" structure was evident, and the microstructure was fully ferritic. The ferrite phase fraction was 100%. Austenite was observed, but in <0.1% of the sample. The fraction of the zero solution was 1.7% and 3.6% for the XY and XZ planes, respectively. The average grain size, however, was smaller than the as-built DSS sample and corresponded to an equivalent circle diameter of 10.5 µm and 11 µm in the XY and XZ planes, respectively. The austenite is shown in blue, ferrite is shown red, and zero solution in white (Figures 17 and 18). The scale bar in all micrographs is 200 µm.

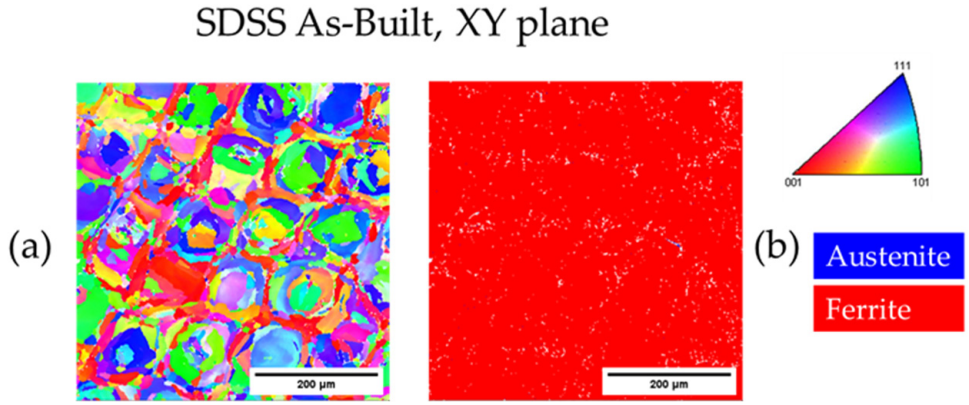

Figure 17. EBSD results of the XY plane in the as-built SDSS sample. (**a**) Inverse pole figure map: <001> directions shown in red; <101> directions in green; <111> directions in blue. (**b**) Phase map.

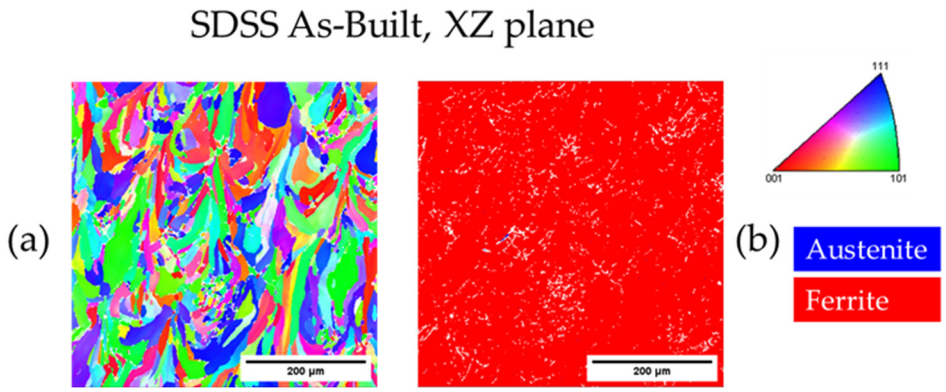

Figure 18. EBSD results of the XZ plane in the as-built SDSS sample. (**a**) Inverse pole figure map: <001> directions shown in red; <101> directions in green; <111> directions in blue. (**b**) Phase map.

3.3.4. Heat-Treated SDSS 2507

In Figures 19 and 20, the stress-relieved and annealed SDSS samples are presented, respectively. As expected, after stress relief heat treatment, no phase transformation took place, and no grain growth or intermetallic phases like sigma and chi could be observed, similar to the as-built DSS sample. A high amount of austenite could be seen in the annealed state, and no melt pool boundaries and laser melt tracks could be identified compared to the as-built microstructure. The annealed and water-quenched microstructure displayed diverse austenite morphologies, such as grain boundary austenite (GBA), intragranular austenite (IGA), and secondary austenite (γ2). Table 8 displays the EDS analysis results of both ferrite and austenite. It was observed that austenite had approximately 5 wt.% higher nickel content compared to ferrite, while ferrite exhibited around 4 wt.% higher chromium content than austenite.

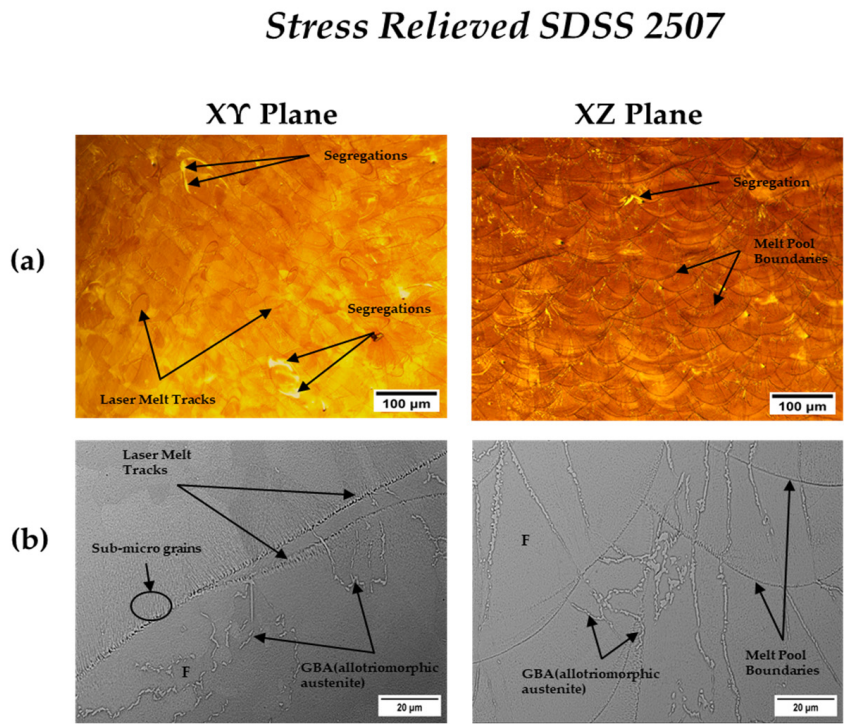

Figure 19. Stress-relieved SDSS microstructure. (**a**) LOM (light optical microscope) and (**b**) SEM (scanning electron microscope) micrographs transverse to build direction (XY plane) and parallel to build direction (XZ plane). F = ferrite; GBA = grain boundary austenite.

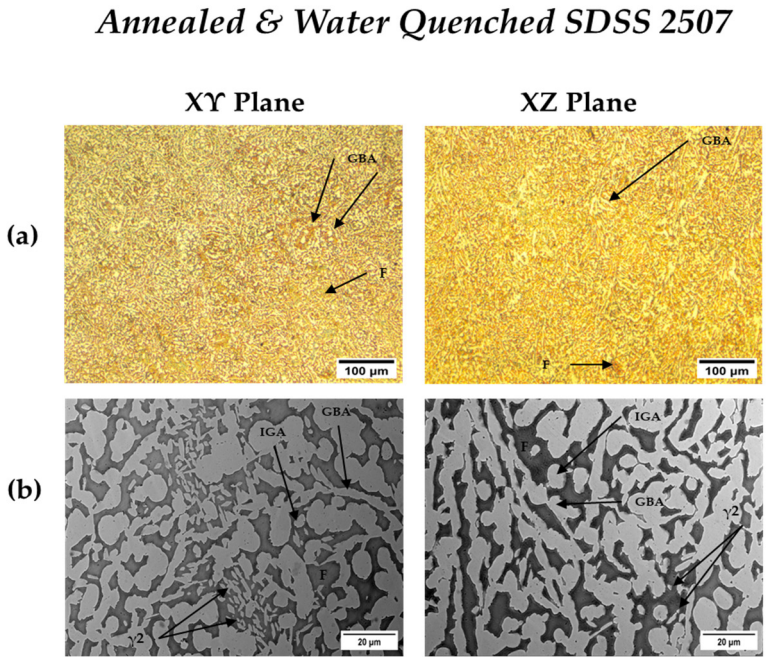

Figure 20. Annealed and water-quenched SDSS microstructure. (**a**) LOM (light optical microscope) and (**b**) SEM (scanning electron microscope) micrographs transverse to build direction (XY plane) and parallel to build direction (XZ plane). F = ferrite; GBA = grain boundary austenite; IGA = intragranular austenite; γ2 = secondary austenite.

Table 8. EDS analysis results of annealed and water-quenched SDSS.

	Elements (wt.%)					
Annealed SDSS	**Si**	**Mn**	**Cr**	**Fe**	**Ni**	**Mo**
Ferrite	0.6	-	27.2	62.0	5.4	4.8
Austenite	-	0.9	23.4	62.5	10.1	3.1

In Figure 21, the results of image analysis indicated a composition of 65% austenite and 35% ferrite for the DSS sample that was subjected to annealing and water quenching.

Figures 22 and 23 show the EBSD IPF and phase maps of the SDSS sample annealed in the XY and XZ planes, respectively. The formation of austenite has changed the microstructure considerably with the austenite grains being fine and well distributed. Yet, the change was different from what had been observed in the annealed and water-quenched DSS sample. The "mosaic" structure was not visible, and the phase fraction of austenite was increased. Specifically, the phase fraction of austenite was 62.8% and 61.8% in the XY and XZ planes, correspondingly, similar to the values obtained via the image analysis method (65%). The fraction of the zero solution was $\leq$1.1% for both planes. Ferrite grains featured a mixed crystallographic orientation along the <001> and <101> crystallographic directions, mostly for both the XY and XZ planes. Austenite grains featured a strong orientation along the <101> crystallographic direction for both the XY and XZ planes. The average grain size corresponded to an equivalent circle diameter of 18 µm and 19 µm for ferrite as seen in the XY and XZ planes, and 3.1 µm and 3.3 µm for austenite as seen in the XY and XZ planes, respectively. The phase fractions and the grain size for all conditions are summarized in Table 9. The grain size is expressed as the diameter of a circle with the same area as the particle (equivalent circle diameter—ECD) in µm.

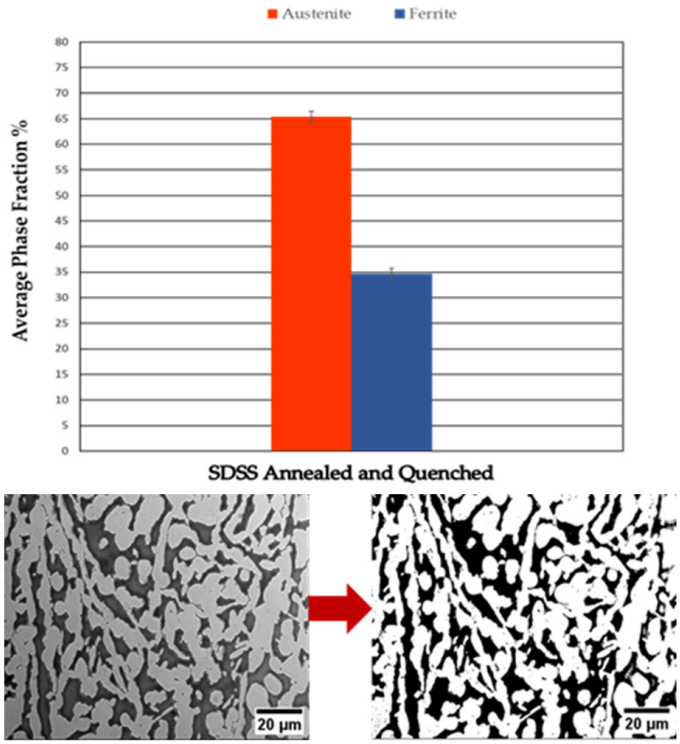

Figure 21. Annealed and water-quenched SDSS image analysis results.

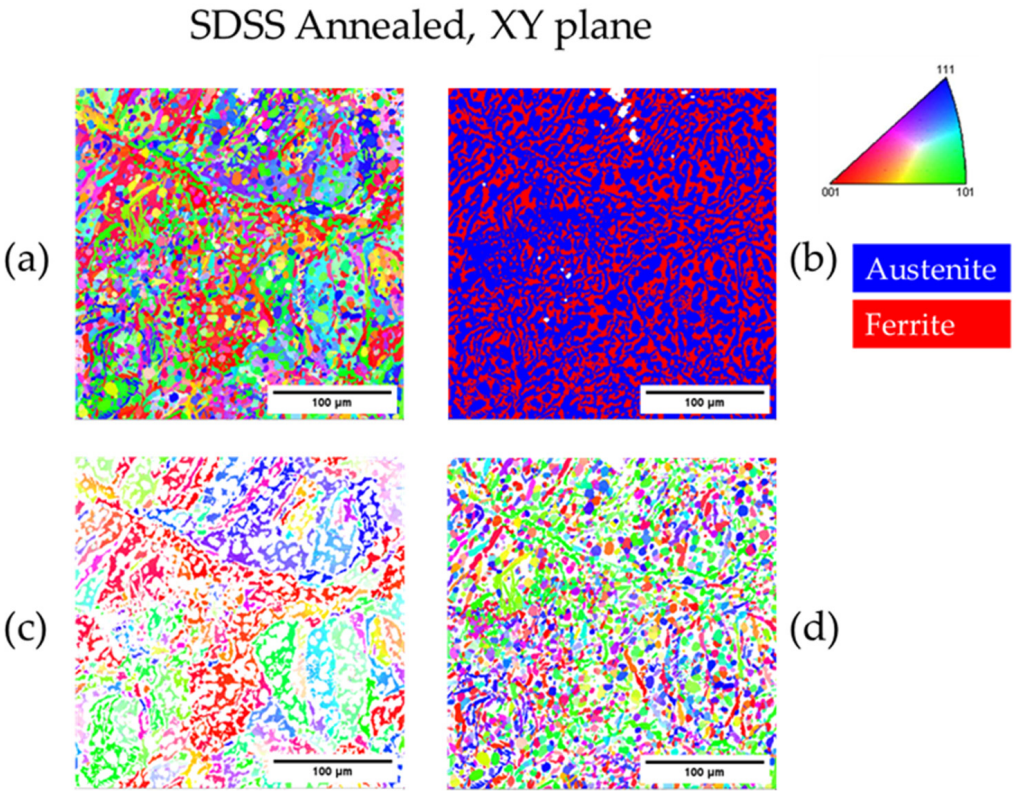

Figure 22. EBSD results of the XY plane in the annealed SDSS sample. (**a**) Inverse pole figure map: <001> directions shown in red; <101> directions in green; <111> directions in blue. (**b**) Phase map. (**c**) Inverse pole figure map for ferrite only. (**d**) Inverse pole figure map for austenite only.

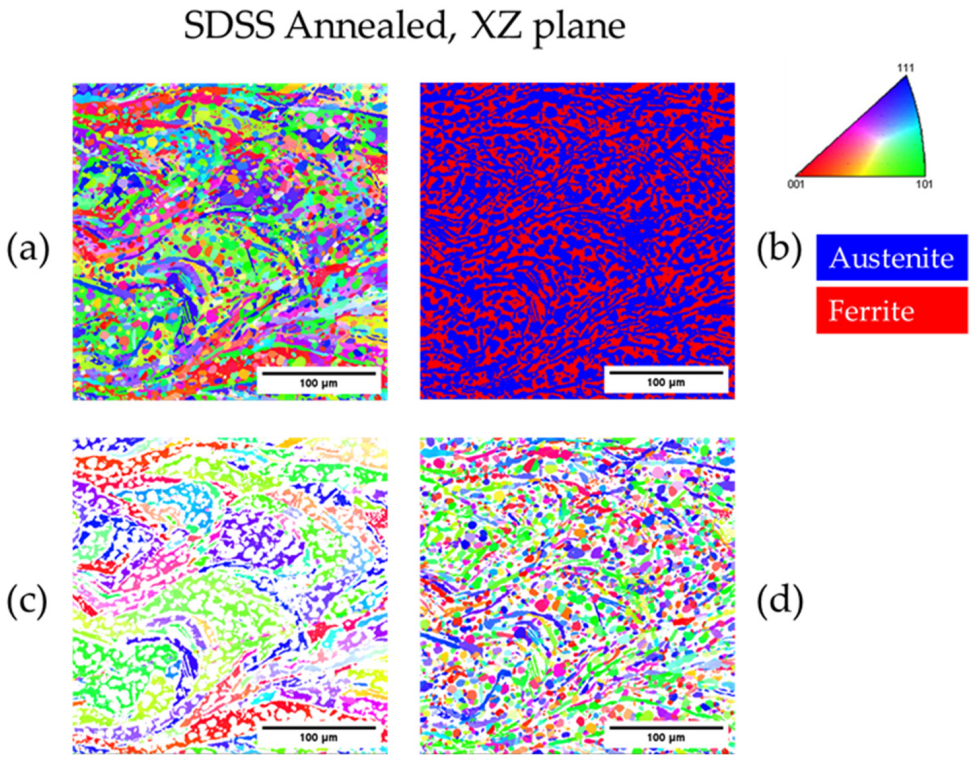

Figure 23. EBSD results of the XZ plane in the annealed SDSS sample. (**a**) Inverse pole figure map: <001> directions shown in red; <101> directions in green; <111> directions in blue. (**b**) Phase map. (**c**) Inverse pole figure map for ferrite only. (**d**) Inverse pole figure map for austenite only.

Table 9. Summary of phase fraction and average grain size in all samples as measured by EBSD for DSS and SDSS alloys.

Sample	Phase Fraction, %		Grain Size (ECD/µm)	
	Austenite	Ferrite	Austenite	Ferrite
As-Built DSS XY	-	100.0	-	12.6
As-Built DSS XZ	-	100.0	-	15.9
As-Built SDSS XY	-	100.0	-	10.5
As-Built SDSS XZ	-	100.0	-	11.0
Annealed DSS XY	31.1	68.9	3.3	22
Annealed DSS XZ	31.6	68.4	3.4	25
Annealed SDSS XY	62.8	37.2	3.1	18
Annealed SDSS XZ	61.8	38.2	3.3	19

3.4. Nanoindentation

The elastic modulus (E) was selected in order to generate the 2D map representation, revealing the difference in nanoindentation response due to phase properties underneath the indenter [25]. In Figure 24, elastic modulus grid maps obtained through nanoindentation are presented. It is evidenced in all cases (DSS and SDSS in both XY and XZ planes) that phase regions of higher E are formed in the annealed samples.

Both hardness (in red) and elastic modulus values (in black) are presented below (Figure 25), in relation to contact depth (residual depth after maximum penetration at 200 nm of displacement), for all samples. All axes are set to specific ranges for comparison; the positioning of the hardness value scatter regarding range (relative) and extent (in contact depth) were attributed to residual stresses occurring in the as-built state (higher H range corresponds to compressive residual stresses [51]), which was also confirmed by the stress-relieving process and plastic deformation, as higher contact depth corresponded to higher plastic deformation.

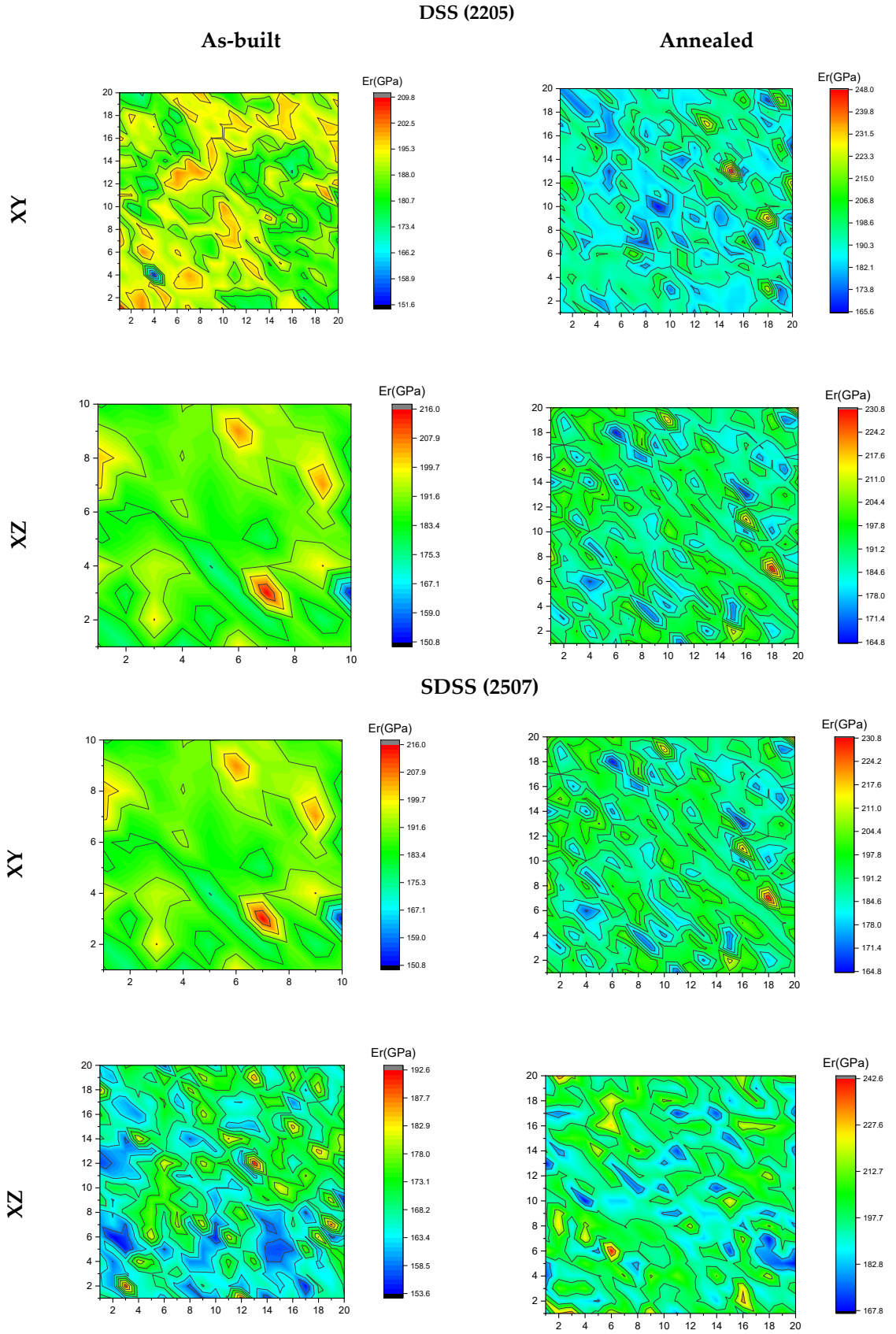

Figure 24. Elastic modulus grid maps obtained through nanoindentation (values in axes correspond to position coordinates).

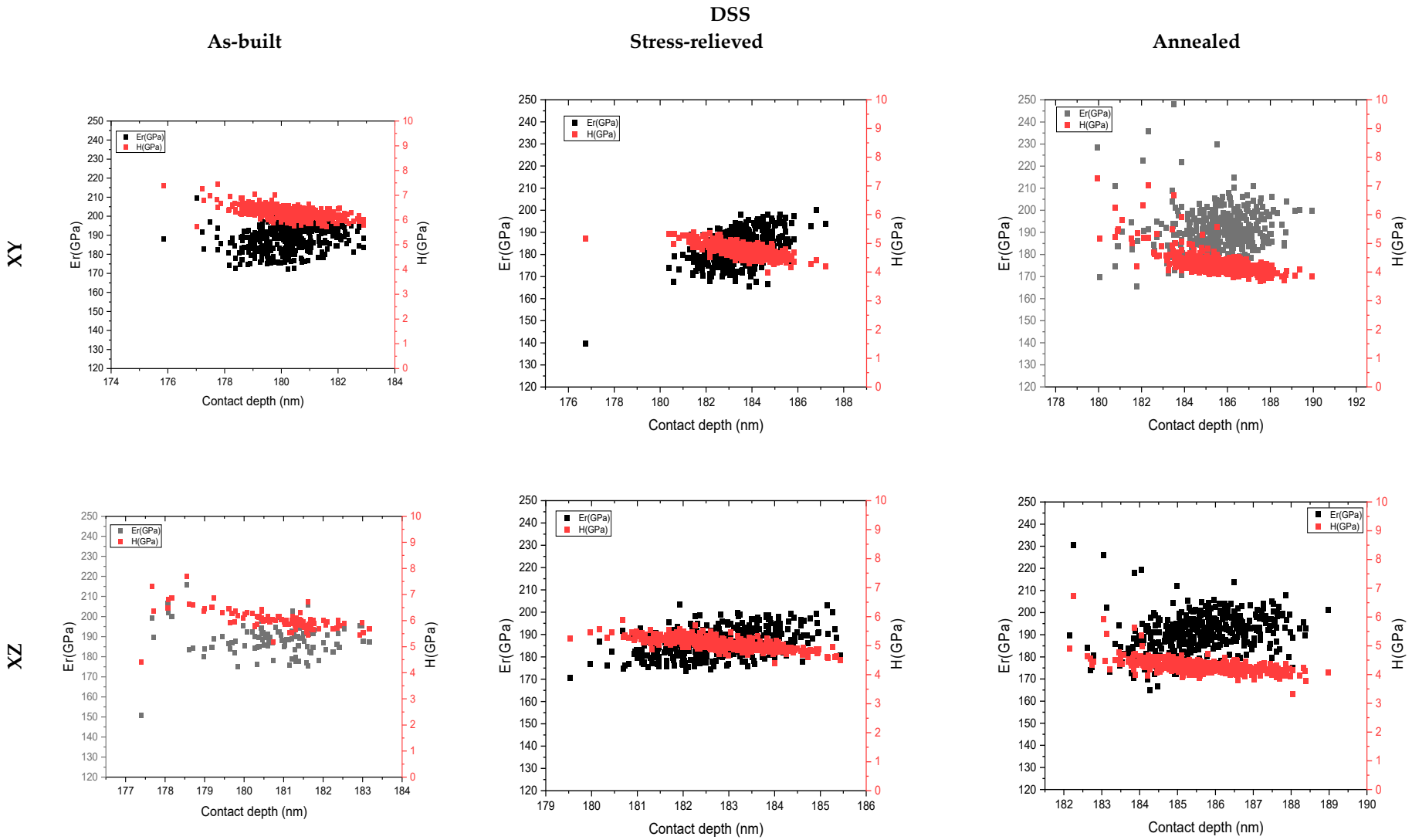

Figure 25. *Cont.*

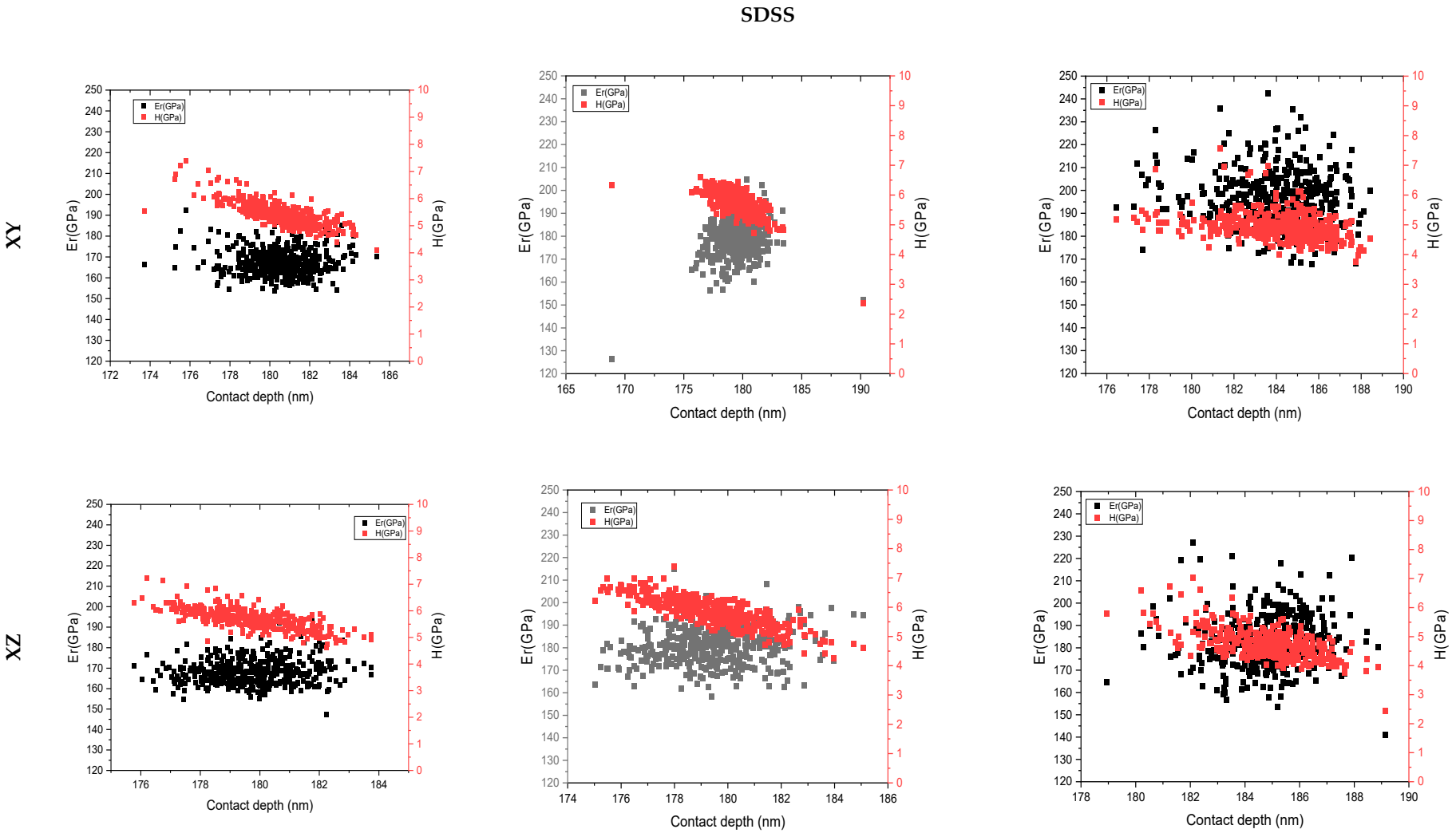

Figure 25. Both hardness (in red) and elastic modulus values (in black) in relation to contact depth (residual depth after maximum penetration at 200 nm of displacement), for all samples.

Ferrite exhibits more noticeable plasticity and residual deformation compared to austenite. This is attributed to the lower yield strength and work-hardening exponent of ferrite in comparison to austenite [46]. Relevant literature studies often draw the conclusion that both ferrite and austenite exhibit identical values measured through nanomechanical testing, which can vary; ferrite has been referenced either to be easier [52] or harder [15] to indent than austenite. In Figure 26, hardness distribution density for all samples is presented in all three states: as-built, stress-relieved, and annealed, respectively. The values corresponded to discrete imprints located within individual phase grains (ferrite and austenite), the combination of the two, and/or regions containing phase boundaries.

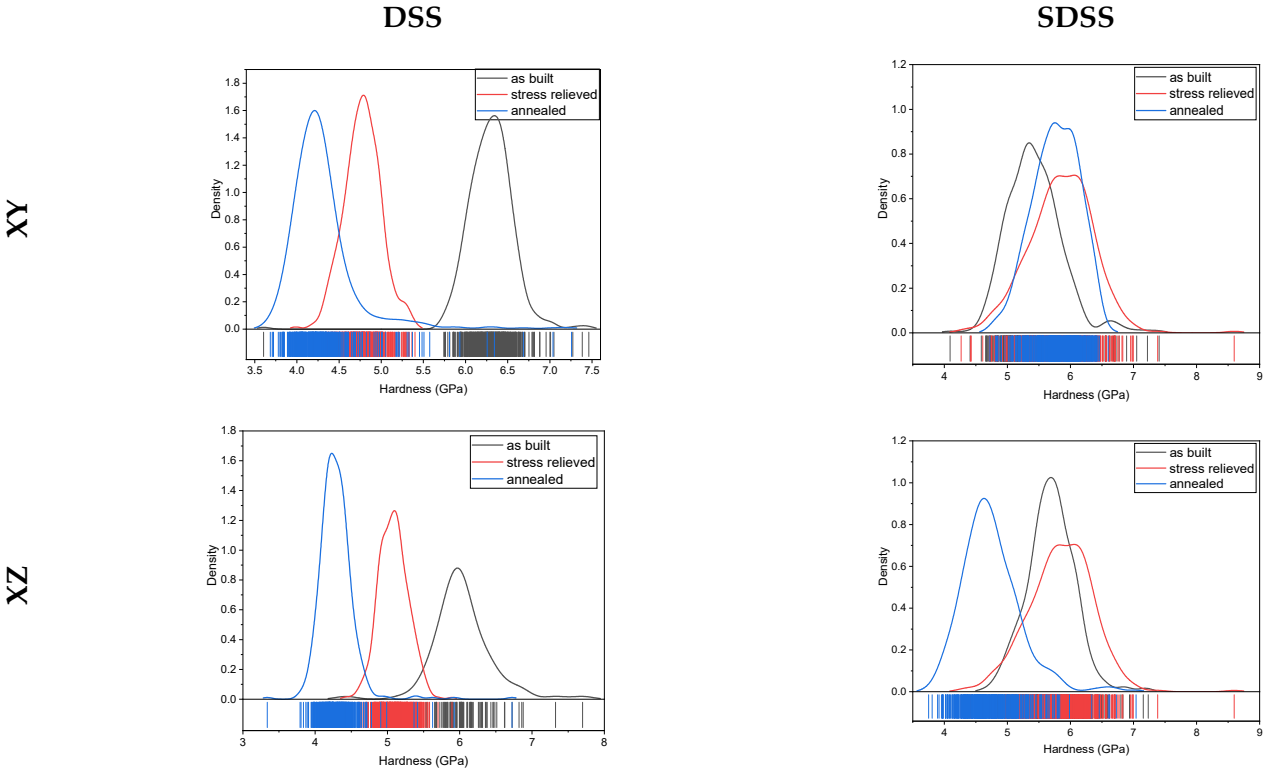

Figure 26. Hardness distribution density for all samples, in all three states: as-built, stress-relieved, and annealed, respectively.

4. Discussion

In LPBF, porosity can be classified into three types: gas pores, keyhole pores, and lack-of-fusion pores. Gas pores, also known as hydrogen porosity, are spherically shaped and small. Keyhole pores are elongated in shape, aligning parallel to the build direction (XZ plane) and appear spherical when viewed from a direction perpendicular to the build direction (XY plane). These pores are also characterized by their large size. Lack-of-fusion pores are also characterized by a large size, often comparable in scale to the melt pool size, and they exhibit irregular shapes. Gas pores are created at slow scanning speeds from gases trapped within the melt pool or evolve from the powder during consolidation. Keyhole pores result from an overabundance of input energy during the melting process. The excessive laser power leads to an over-penetration of the metal powder, leaving a pore near the base of the solidified melt pool. In contrast, lack-of-fusion pores originate from an insufficient supply of energy to the powder bed during the melting process. This reduced energy input results in the incomplete melting of the metal powder, leading to the formation of voids within the final structure [52–54]. In Figures 5 and 6, it was observed that pores originating from lack of fusion decreased with an increase in VED, while maintaining the other two parameters stable. However, the occurrence of lack-of-fusion pores increased notably when the hatch distance was increased, especially when the VED and scan speed

were maintained at 50 J/mm^3 and 1000 mm/s, respectively. Nevertheless, an excessive increase in VED (>80 J/mm^3) resulted in the formation of keyhole pores. All types of pores were decreased when the hatch distance and scan speed values were near 100–110 µm and 1100 mm/s, correspondingly, with VED values close to 60 J/mm^3. In the current study, the optimal LPBF process variables and VED yielding near-fully dense samples were identified, also taking into account the physical and morphological DSS and SDSS powder characteristics (lack of internal pores, agglomerates, contaminations, elongated particles, and PSD values within specifications). The inherent high cooling rates of the LPBF process resulted in ferrite nucleation and growth because there was not sufficient time for austenite formation through solid-state diffusion. This resulted in nearly zero content of austenite in the microstructure of DSS (Figure 8) and very low austenite content in the microstructure of the SDSS sample (Figure 16). EBSD phase maps displayed a 100% ferrite volume fraction in the as-built microstructure of both alloys. In the SDSS sample, the EBSD phase maps (Figures 17 and 18) exhibited a higher fraction of the zero solution in comparison with the DSS EBSD phase maps (Figures 9 and 10). The higher percentage of the zero solution in the SDSS microstructure may be attributed to the micro-crystalline GBA, which was observed in the SEM micrographs (Figure 16b). It has been reported that phases with concentrations below 5%, including chromium nitrides, micro-crystalline austenite, and process-related defects, such as pores and cracks, are identified by the EBSD detector as a fraction of zero solutions. Therefore, they are excluded from the calculation of the ferrite and austenite phase fraction [18]. The crystallographic orientation is influenced by the LPBF process parameters [34]. Therefore, they are excluded from the calculation of the ferrite and austenite phase fraction [18]. In this case, the DSS and SDSS process parameters of optimum samples were almost identical in terms of laser power, scan speed, and hatch distance. Thus, ferrite grains of DSS and SDSS in the as-built microstructures had a similar mixed crystallographic orientation (Figures 9, 10, 17 and 18). The 67-rotation scanning strategy resulted in crystallographic anisotropy of the as-built samples [38]. The ECD average grain size of the as-built SDSS sample was slightly smaller than that of the as-built DSS sample (Table 9).

The presence of austenite in the as-built SDSS microstructure can be attributed to the higher Ni content in the feedstock material in comparison to DSS (Table 1). This, in conjunction with the secondary energy input from the melting and cooling of the subsequent layers (reheating), allows sufficient time for the formation of a higher volume fraction of the austenite phase in SDSS [55]. Heat-affected areas or heat-affected zones (HAZs) were observed between and near the overlaps of laser melt tracks. An increased austenite presence was observed in HAZs (Figure 16b). Reheating promotes the nucleation and growth of grain boundary austenite that nucleates first at high temperatures (1350–800 °C) [56]. In this experimental analysis, intermetallic phases were not observed. Nonetheless, previous research has documented the presence of chromium nitride precipitation in the as-built microstructure of DSS, which was identified and observed using transmission electron microscopy (TEM) [20]. Studies indicate that elevated nitrogen content in duplex stainless steels can lead to an increased presence of chromium nitrides due to non-equilibrium cooling rates [57]. Hence, it is reasonable to assume the presence of chromium nitrides in the microstructure of DSS and SDSS.

Furthermore, the as-built microstructure of SDSS revealed the presence of micro-segregation and sub-micro-grain regions. EDS analysis indicated that the segregation areas exhibited a high nickel content. This segregation phenomenon can be attributed to the complex flow dynamics within the melt pool, driven by forces such as Marangoni, buoyancy, gravity, and recoil pressure [58]. Elemental segregation in additively manufactured samples can significantly influence corrosion resistance [59]. Sub-micro-grain zones near the melt pool and laser melt track boundaries were observed due to constitutional supercooling coupled with rapid solidification [60]. Research has shown that the formation of fine sub-micro-grains during the LPBF process enhances the yield strength of as-built SS316L [61].

Interestingly, in the as-built microstructure of DSS, no evidence of micro-segregation or sub-micro-grain regions was found.

In the case of the heat-treated samples, the stress-relieved samples (Figures 11 and 19) exhibited no significant microstructural changes when compared to the as-built DSS (Figure 8) and SDSS (Figure 16) samples. However, the annealed and water-quenched samples (Figures 12 and 20) exhibited distinct microstructural changes when compared to the as-built DSS and SDSS samples. These changes included the nucleation and growth of austenite, as well as the removal of melt pool boundaries and laser melt tracks. The annealing process at 1100 °C for 1 h led to a homogenized as-built SDSS microstructure by dissolving the segregations. Annealing also triggered the nucleation and growth of grain boundary austenite (GBA) and intragranular (IGA) and secondary γ2 austenite inside the ferrite grains. IGA and γ2 were observed within the ferritic grains as well as between the GBA (Figures 12 and 20). Notably, in comparison to GBA, the formation of IGA and γ2 occurred at lower temperatures due to the higher activation energy required for their lattice diffusion [56,62,63].

Based on phase quantification obtained from SEM micrographs and EBSD analysis, SDSS exhibited a significantly higher austenite volume fraction (approximately 60% austenite) compared to DSS (approximately 30% austenite) when subjected to the same solution annealing process. This difference can be attributed to the higher nickel and nitrogen content in the SDSS chemical composition, which induced austenite nucleation as per the Ni equivalent formula of the WRC-1992 diagram [64]. During the heat treatment process, it is likely that chromium nitrides will dissolve. The nitrogen from these dissolved chromium nitrides, along with the nitrogen trapped within the ferrite matrix, will diffuse and contribute to the formation of austenite [15]. Grain size analysis revealed that both DSS and SDSS samples, which underwent annealing and quenching, exhibited a similar austenite grain size (with an average grain size of approximately 3 μm). However, the SDSS sample subjected to annealing and quenching displayed marginally smaller ferrite grains compared to the DSS sample that underwent the same treatment (Table 9). In the annealed and quenched SDSS sample, the austenitic grains predominantly exhibited a <101> crystallographic orientation, whereas the annealed and quenched DSS sample displayed a mixed crystallographic orientation. As for the ferritic grains, both DSS and SDSS samples subjected to annealing and quenching showed a mixed crystallographic orientation, with <001> and <101> being the prevailing crystallographic directions.

During the LPBF procedure, the intensive localized heating and rapid cooling of a melt pool, in addition to the layer-by-layer repetition of such a thermomechanical process, result in significant thermal gradients and heterogeneous residual stresses within a non-equilibrium microstructure [65–68]. The magnitude of these thermal gradients is influenced by many processing parameters, including bed temperature, laser power, metal powder morphology, thermophysical characteristics, extent of melt pool, etc. The synergistic occurrence of these parameters often results in a complex residual stress field. Studies of the macroscale residual stresses in AM materials have revealed various deleterious effects (e.g., loss of net shape, detachment from support structures, or failure of the build parts, etc.). However, how (and to what extent) microscale residual stresses influence the mechanical performance of AM materials, remain elusive [69] and are attributed to the difficulty in the measurement and understanding of the spatiotemporal evolution of residual stresses at the scale of individual grains or phases. Through the nanoindentation measurements conducted in this study, a higher contact depth range, which corresponds to higher plastic deformation, was revealed for the annealed state; in the stress relief state, the XY plane exhibited a narrower range denoting a robust deformation mechanism for both DSS and SDSS samples. For DSS, the hardness distribution in the XY plane revealed a gradual decrease when subjected to stress relief (avg. ~4.8 GPa), denoting compressive residual stresses in the as-built state (avg. ~6.3 GPa); hardness was decreased with high-temperature annealing and quenching (avg. ~4.3 GPa). For the XZ plane, the hardness distribution revealed a gradual decrease when subjected to stress relief (avg. ~5.08 GPa), denoting

compressive residual stresses in the as-built state (avg. ~6 GPa); hardness decreased with annealing (avg. ~4.3 GPa), reaching the value of the XY plane. For SDSS, in both planes, the hardness distribution did not reveal significant changes in the as-built or stress relief condition. Also, there was no reduction in hardness for the as-built SDSS sample (avg. ~5.7 GPa) when subjected to stress relief annealing (avg ~5.8 GPa). The high-temperature annealing reduced the hardness of the as-built SDSS sample (avg. ~4.8 GPa). The reduction in average hardness in the annealed condition can be explained by the presence of austenite in the microstructure of both alloys. The higher hardness in the as-built state of both alloys can also be explained by the high dislocation density inside the material that results in hardening [50]. Moreover, chromium nitride precipitates can inhibit free dislocation slip/glide and contribute to hardening. The solubility of N in ferrite leads to solid solution strengthening. The precipitation of chromium nitrides increases the yield and tensile strength [70]. In contrast to the grains in the horizontal plane (XY), grains in the lateral and frontal planes (XZ and YZ) are expected to be elongated [71]. This is attributed to the thermal gradient being higher in the vertical (build) direction of the printed part. Consequently, the grains are expected to grow along several layers, and therefore give rise to elongated types of grains.

5. Conclusions

The current study demonstrated the successful fabrication of duplex and super duplex stainless steels processed via laser powder bed fusion with a nearly balanced austenite–ferrite arrangement after suitable heat treatment. In the as-built condition, both DSS and SDSS exhibited a predominantly ferritic microstructure (~100%) attributed to the high cooling rates suppressing austenite nucleation. In the as-built SDSS microstructure, a trace of grain boundary austenite was evident, along with micro-segregations and cellular grains due to the melt pool driving forces and rapid solidification. The ferrite grains in the as-built DSS and SDSS samples displayed a mixed crystallographic orientation. Solution annealing at 1100 °C for 1 h contributed to austenite recovery in both the DSS and SDSS microstructures. SDSS exhibited a higher degree of austenite in its annealed and quenched microstructure (~60% austenite volume fraction), facilitated by its higher nickel and nitrogen content compared to DSS (~30% austenite volume fraction). In the annealed and water-quenched microstructure of SDSS, the austenitic grains aligned predominantly along the <101> crystallographic direction, while in the annealed and quenched microstructure of DSS, they displayed a more varied orientation. The stress-relieved samples retained the same microstructure as the as-built samples, with no intermetallic phases or carbides/nitrides observed in either the heat-treated or as-built microstructures using the methods and tools employed in this study. Nanoindentation was utilized to obtain hardness and modulus values, providing insights into the nanomechanical response of the selected materials in all three conditions. This method effectively revealed phase regions with higher E values after annealing, indicating new phase formation. The annealed state exhibited greater contact depth (~181–189 nm) and plastic deformation due to austenite nucleation and growth, while the stress-relieved state showed a narrower range in the XY plane (DSS: ~181–185 nm and SDSS: ~178–182 nm), indicating a more robust deformation mechanism for both DSS and SDSS samples. The hardness distribution analysis quantified the effect of the stress relief protocol in all cases.

Author Contributions: Conceptualization, L.G. and E.K.K.; methodology, L.G. and E.K.K.; formal analysis, L.G. and L.K.; data curation, L.K. and J.S.G.; writing—original draft preparation, L.G. and L.K.; writing—review and editing, L.G., L.K., J.S.G., S.D., E.P.K. and E.K.K.; supervision, E.K.K.; project administration, E.K.K.; funding acquisition, E.K.K. All authors have read and agreed to the published version of the manuscript.

Funding: This research was funded by the European Commission under the HORIZON2020 Framework Programme Grant Agreement no. 952869. This research was conducted within the framework of Nanomecommons project. https://www.nanomecommons.net/ (accessed on 13 November 2023).

Data Availability Statement: Data are contained within the article.

Conflicts of Interest: The authors declare no conflict of interest. The funders had no role in the design of the study; in the collection, analysis or interpretation of data; in the writing of the manuscript; or in the decision to publish the results.

References

1. Francis, R.; Byrne, G. Duplex Stainless Steels—Alloys for the 21st Century. *Metals* **2021**, *11*, 836. [CrossRef]
2. Sharma, L.; Sharma, K. Dissimilar welding of super duplex stainless steel (SDSS) and pipeline steel—A brief overview. *Mater. Today Proc.* **2022**. [CrossRef]
3. Khan, W.N.; Chhibber, R. Effect of filler metal on solidification, microstructure and mechanical properties of dissimilar super duplex/pipeline steel GTA weld. *Mater. Sci. Eng. A* **2021**, *803*, 140476. [CrossRef]
4. Gatto, M.L.; Cerqueni, G.; Groppo, R.; Tognoli, E.; Santoni, A.; Cabibbo, M.; Mattioli-Belmonte, M.; Mengucci, P. On the Biomechanical Performances of Duplex Stainless Steel Graded Scaffolds Produced by Laser Powder Bed Fusion for Tissue Engineering Applications. *J. Funct. Biomater.* **2023**, *14*, 489. [CrossRef]
5. Gatto, M.L.; Santoni, A.; Santecchia, E.; Spigarelli, S.; Fiori, F.; Mengucci, P.; Cabibbo, M. The Potential of Duplex Stainless Steel Processed by Laser Powder Bed Fusion for Biomedical Applications: A Review. *Metals* **2023**, *13*, 949. [CrossRef]
6. Alvarez-Armas, I.; Degallaix-Moreuil, S. *Duplex Stainless Steels*; Wiley: Hoboken, NJ, USA, 2013.
7. Gunn, R.N. (Ed.) 1—Developments, grades and specifications. In *Duplex Stainless Steels—Microstructure, Properties and Applications*; Woodhead Publishing: Sawston, UK, 1997; pp. 1–13.
8. Chail, G.; Kangas, P. Super and hyper duplex stainless steels: Structures, properties and applications. *Procedia Struct. Integr.* **2016**, *2*, 1755–1762. [CrossRef]
9. Davidson, K.; Singamneni, S. Selective Laser Melting of Duplex Stainless Steel Powders: An Investigation. *Mater. Manuf. Process.* **2016**, *31*, 1543–1555. [CrossRef]
10. Zhang, Y.; Wu, S.; Cheng, F. A specially-designed super duplex stainless steel with balanced ferrite:austenite ratio fabricated via flux-cored wire arc additive manufacturing: Microstructure evolution, mechanical properties and corrosion resistance. *Mater. Sci. Eng. A* **2022**, *854*, 143809. [CrossRef]
11. Pantelakis, S.; Eriksson, M.; Lervåg, M.; Sørensen, C.; Robertstad, A.; Brønstad, B.M.; Nyhus, B.; Aune, R.; Ren, X.; Akselsen, O.M.; et al. Additive manufacture of superduplex stainless steel using WAAM. *MATEC Web Conf.* **2018**, *188*, 03014. [CrossRef]
12. Sayyar, N.; Hansen, V.; Tucho, W.M.; Minde, M.W. Directed laser deposition of super duplex stainless steel: Microstructure, texture evolution, and mechanical properties. *Heliyon* **2023**, *9*, e15144. [CrossRef]
13. Zitelli, C.; Folgarait, P.; Di Schino, A. Laser Powder Bed Fusion of Stainless Steel Grades: A Review. *Metals* **2019**, *9*, 731. [CrossRef]
14. Cobbinah, P.V.; Nzeukou, R.A.; Onawale, O.T.; Matizamhuka, W.R. Laser Powder Bed Fusion of Potential Superalloys: A Review. *Metals* **2020**, *11*, 58. [CrossRef]
15. Hengsbach, F.; Koppa, P.; Duschik, K.; Holzweissig, M.J.; Burns, M.; Nellesen, J.; Tillmann, W.; Tröster, T.; Hoyer, K.-P.; Schaper, M. Duplex stainless steel fabricated by selective laser melting—Microstructural and mechanical properties. *Mater. Des.* **2017**, *133*, 136–142. [CrossRef]
16. Mulhi, A.; Dehgahi, S.; Waghmare, P.; Qureshi, A.J. Process Parameter Optimization of 2507 Super Duplex Stainless Steel Additively Manufactured by the Laser Powder Bed Fusion Technique. *Metals* **2023**, *13*, 725. [CrossRef]
17. Xiang, H.; Chen, G.; Zhao, W.; Wu, C. Densification Behavior and Build Quality of Duplex Stainless Steel Fabricated by Laser Powder Bed Fusion. *Metals* **2023**, *13*, 741. [CrossRef]
18. Raffeis, I.; Vroomen, U.; Adjei-Kyeremeh, F.; Großmann, D.; Hammelrath, H.; Westhoff, E.; Bremen, S.; Boscolo Bozza, D.; Bhrig-Polaczek, A. Comparative investigations into microstructural and mechanical properties of as-cast and laser powder bed fusion (LPBF) fabricated duplex steel (1.4517). *Mater. Und Werkst.* **2020**, *51*, 432–444. [CrossRef]
19. Davidson, K.P.; Singamneni, S.B. Metallographic evaluation of duplex stainless steel powders processed by selective laser melting. *Rapid Prototyp. J.* **2017**, *23*, 1146–1163. [CrossRef]
20. Haghdadi, N.; Ledermueller, C.; Chen, H.; Chen, Z.; Liu, Q.; Li, X.; Rohrer, G.; Liao, X.; Ringer, S.; Primig, S. Evolution of microstructure and mechanical properties in 2205 duplex stainless steels during additive manufacturing and heat treatment. *Mater. Sci. Eng. A* **2022**, *835*, 142695. [CrossRef]
21. Freitas, B.J.M.; Rodrigues, L.C.M.; Claros, C.A.E.; Botta, W.J.; Koga, G.Y.; Bolfarini, C. Ferritic-induced high-alloyed stainless steel produced by laser powder bed fusion (L-PBF) of 2205 duplex stainless steel: Role of microstructure, corrosion, and wear resistance. *J. Alloy. Compd.* **2022**, *918*, 165576. [CrossRef]
22. Freitas, G.C.L.D.; Fonseca, G.S.d.; Moreira, L.P.; Leite, D.N.F. Phase transformations of the duplex stainless steel UNS S31803 under non-isothermal conditions. *J. Mater. Res. Technol.* **2021**, *11*, 1847–1851. [CrossRef]
23. Kashiwar, A.; Vennela, N.P.; Kamath, S.L.; Khatirkar, R.K. Effect of solution annealing temperature on precipitation in 2205 duplex stainless steel. *Mater. Charact.* **2012**, *74*, 55–63. [CrossRef]
24. Mampuya, M.B.; Umba, M.C.; Mutombo, K.; Olubambi, P.A. Effect of heat treatment on the microstructure of duplex stainless steel 2205. *Mater. Today Proc.* **2021**, *38*, 1107–1112. [CrossRef]

25. Gargalis, L.; Karavias, L.; Graff, J.S.; Diplas, S.; Koumoulos, E.P.; Karaxi, E.K. Novel Powder Feedstock towards Microstructure Engineering in Laser Powder Bed Fusion: A Case Study on Duplex/Super Duplex and Austenitic Stainless-Steel Alloys. *Metals* **2023**, *13*, 1546. [CrossRef]
26. Cui, C.; Becker, L.; Gärtner, E.; Boes, J.; Lentz, J.; Uhlenwinkel, V.; Steinbacher, M.; Weber, S.; Fechte-Heinen, R. Laser Additive Manufacturing of Duplex Stainless Steel via Powder Mixture. *J. Manuf. Mater. Process.* **2022**, *6*, 72. [CrossRef]
27. Köhler, M.L.; Kunz, J.; Herzog, S.; Kaletsch, A.; Broeckmann, C. Microstructure analysis of novel LPBF-processed duplex stainless steels correlated to their mechanical and corrosion properties. *Mater. Sci. Eng. A* **2021**, *801*, 140432. [CrossRef]
28. Nilsson, J.O. Super duplex stainless steels. *Mater. Sci. Technol.* **1992**, *8*, 685–700. [CrossRef]
29. Steiner Petrovič, D.; Pirnat, M.; Klančnik, G.; Mrvar, P.; Medved, J. The effect of cooling rate on the solidification and microstructure evolution in duplex stainless steel. *J. Therm. Anal. Calorim.* **2012**, *109*, 1185–1191. [CrossRef]
30. Narasimharaju, S.R.; Zeng, W.; See, T.L.; Zhu, Z.; Scott, P.; Jiang, X.; Lou, S. A comprehensive review on laser powder bed fusion of steels: Processing, microstructure, defects and control methods, mechanical properties, current challenges and future trends. *J. Manuf. Process.* **2022**, *75*, 375–414. [CrossRef]
31. David, S.A.; Vitek, J.M.; Reed, R.W.; Hebble, T.L. *Effect of Rapid Solidification on Stainless Steel Weld Metal Microstructures and Its Implications on the Schaeffler Diagram*; Oak Ridge National Lab. (ORNL): Oak Ridge, TN, USA, 1987.
32. Saeidi, K.; Kevetkova, L.; Lofaj, F.; Shen, Z. Novel ferritic stainless steel formed by laser melting from duplex stainless steel powder with advanced mechanical properties and high ductility. *Mater. Sci. Eng. A* **2016**, *665*, 59–65. [CrossRef]
33. Xie, C.; Li, B.; Liu, G.; Liu, J.; Ying, H.; Li, D.; Wang, S.; Wang, L. Study on the effect of solution treatment on mechanical and corrosion properties of SAF 2507DSS produced by LPBF. *J. Mater. Res. Technol.* **2023**, *26*, 2070–2081. [CrossRef]
34. Nigon, G.N.; Burkan Isgor, O.; Pasebani, S. The effect of annealing on the selective laser melting of 2205 duplex stainless steel: Microstructure, grain orientation, and manufacturing challenges. *Opt. Laser Technol.* **2021**, *134*, 106643. [CrossRef]
35. Llorca-Isern, N.; López-Luque, H.; López-Jiménez, I.; Biezma, M.V. Identification of sigma and chi phases in duplex stainless steels. *Mater. Charact.* **2016**, *112*, 20–29. [CrossRef]
36. Knyazeva, M.; Pohl, M. Duplex Steels. Part II: Carbides and Nitrides. *Metallogr. Microstruct. Anal.* **2013**, *2*, 343–351. [CrossRef]
37. Di Cocco, V.; Iacoviello, F.; Ischia, G. Duplex stainless steels "475 °C embrittlement": Influence of the chemical composition on the fatigue crack propagation. *Procedia Struct. Integr.* **2017**, *3*, 299–307. [CrossRef]
38. Papula, S.; Song, M.; Pateras, A.; Chen, X.B.; Brandt, M.; Easton, M.; Yagodzinskyy, Y.; Virkkunen, I.; Hanninen, H. Selective Laser Melting of Duplex Stainless Steel 2205: Effect of Post-Processing Heat Treatment on Microstructure, Mechanical Properties, and Corrosion Resistance. *Materials* **2019**, *12*, 2468. [CrossRef] [PubMed]
39. Xiang, H.; Zhao, W.; Lu, Y. Effect of solution temperature on microstructure and mechanical properties of selective laser melted Fe–22Cr–5Ni-0.26N duplex stainless steel. *J. Mater. Res. Technol.* **2022**, *19*, 1379–1389. [CrossRef]
40. Hosseini, A.; Karlsson, V.; Örnek, L.; Reccagni, C.; Wessman, P.; Engelberg, S.D. Microstructure and functionality of a uniquely graded super duplex stainless steel designed by a novel arc heat treatment method. *Mater. Charact.* **2018**, *139*, 390–400. [CrossRef]
41. Moallemi, M.; Zarei-Hanzaki, A.; Kim, S.-J.; Alimadadi, H. On the microstructural-textural characterization and deformation analysis of a nano/ultrafine grained Fe-20Cr-8Mn-0.3N duplex alloy with superior mechanical properties. *Mater. Charact.* **2019**, *156*, 109878. [CrossRef]
42. Wang, X.F.; Yang, X.P.; Guo, Z.D.; Zhou, Y.C.; Song, H.W. Nanoindentation Characterization of Mechanical Properties of Ferrite and Austenite in Duplex Stainless Steel. *Adv. Mater. Res.* **2007**, *26–28*, 1165–1170. [CrossRef]
43. *ISO 13322-1:2014*; Particle Size Analysis Image Analysis Methods Part 1: Static Image Analysis Methods. ISO: London, UK, 2014.
44. A Hosseini, V.; Hurtig, K.; Eyzop, D.; Östberg, A.; Janiak, P.; Karlsson, L. Ferrite content measurement in super duplex stainless steel welds. *Weld. World* **2019**, *63*, 551–563. [CrossRef]
45. Oliver, W.C.; Pharr, G.M. An improved technique for determining hardness and elastic modulus using load and displacement sensing indentation experiments. *J. Mater. Res.* **1992**, *7*, 1564–1583. [CrossRef]
46. Tao, P.; Gong, J.-m.; Wang, Y.-f.; Jiang, Y.; Li, Y.; Cen, W.-w. Characterization on stress-strain behavior of ferrite and austenite in a 2205 duplex stainless steel based on nanoindentation and finite element method. *Results Phys.* **2018**, *11*, 377–384. [CrossRef]
47. Vincent, C.; Silvain, J.F.; Heintz, J.M.; Chandra, N. Effect of porosity on the thermal conductivity of copper processed by powder metallurgy. *J. Phys. Chem. Solids* **2012**, *73*, 499–504. [CrossRef]
48. Yi, F.; Zhou, Q.; Wang, C.; Yan, Z.; Liu, B. Effect of powder reuse on powder characteristics and properties of Inconel 718 parts produced by selective laser melting. *J. Mater. Res. Technol.* **2021**, *13*, 524–533. [CrossRef]
49. Akram, J.; Chalavadi, P.; Pal, D.; Stucker, B. Understanding grain evolution in additive manufacturing through modeling. *Addit. Manuf.* **2018**, *21*, 255–268. [CrossRef]
50. Haghdadi, N.; Laleh, M.; Moyle, M.; Primig, S. Additive manufacturing of steels: A review of achievements and challenges. *J. Mater. Sci.* **2021**, *56*, 64–107. [CrossRef]
51. Charitidis, C.A.; Dragatogiannis, D.A.; Koumoulos, E.P.; Kartsonakis, I.A. Residual stress and deformation mechanism of friction stir welded aluminum alloys by nanoindentation. *Mater. Sci. Eng. A* **2012**, *540*, 226–234. [CrossRef]
52. Ferro, P.; Meneghello, R.; Savio, G.; Berto, F. A modified volumetric energy density–based approach for porosity assessment in additive manufacturing process design. *Int. J. Adv. Manuf. Technol.* **2020**, *110*, 1911–1921. [CrossRef]
53. Snell, R.; Tammas-Williams, S.; Chechik, L.; Lyle, A.; Hernández-Nava, E.; Boig, C.; Panoutsos, G.; Todd, I. Methods for Rapid Pore Classification in Metal Additive Manufacturing. *Jom* **2019**, *72*, 101–109. [CrossRef]

54. Ghayoor, M.; Lee, K.; He, Y.; Chang, C.-h.; Paul, B.K.; Pasebani, S. Selective laser melting of 304L stainless steel: Role of volumetric energy density on the microstructure, texture and mechanical properties. *Addit. Manuf.* **2020**, *32*, 101011. [CrossRef]
55. Chowdhury, S.; Yadaiah, N.; Prakash, C.; Ramakrishna, S.; Dixit, S.; Gupta, L.R.; Buddhi, D. Laser powder bed fusion: A state-of-the-art review of the technology, materials, properties & defects, and numerical modelling. *J. Mater. Res. Technol.* **2022**, *20*, 2109–2172. [CrossRef]
56. Zhang, Z.; Jing, H.; Xu, L.; Han, Y.; Zhao, L. Investigation on microstructure evolution and properties of duplex stainless steel joint multi-pass welded by using different methods. *Mater. Des.* **2016**, *109*, 670–685. [CrossRef]
57. Zhang, B.; Li, H.; Zhang, S.; Jiang, Z.; Lin, Y.; Feng, H.; Zhu, H. Effect of nitrogen on precipitation behavior of hyper duplex stainless steel S32707. *Mater. Charact.* **2021**, *175*, 111096. [CrossRef]
58. Xianfeng, X.; Cong, L.; Yanshu, F.; Xiaojun, Y.; Lijun, S. Progress on Experimental Study of Melt Pool Flow Dynamics in Laser Material Processing. In *Liquid Metals*; Samson Jerold Samuel, C., Gnanasekaran, S., Suresh, M., Eds.; IntechOpen: Rijeka, Croatia, 2021; p. Ch.3.
59. Shang, C.; Wu, H.; Pan, G.; Zhu, J.; Wang, S.; Wu, G.; Gao, J.; Liu, Z.; Li, R.; Mao, X. The Characteristic Microstructures and Properties of Steel-Based Alloy via Additive Manufacturing. *Materials* **2023**, *16*, 2696. [CrossRef] [PubMed]
60. Tan, C.; Zhou, K.; Kuang, M.; Ma, W.; Kuang, T. Microstructural characterization and properties of selective laser melted maraging steel with different build directions. *Sci. Technol. Adv. Mater.* **2018**, *19*, 746–758. [CrossRef]
61. Wang, Y.M.; Voisin, T.; McKeown, J.T.; Ye, J.; Calta, N.P.; Li, Z.; Zeng, Z.; Zhang, Y.; Chen, W.; Roehling, T.T.; et al. Additively manufactured hierarchical stainless steels with high strength and ductility. *Nat. Mater.* **2018**, *17*, 63–71. [CrossRef]
62. Verma, J.; Taiwade, R.V. Effect of welding processes and conditions on the microstructure, mechanical properties and corrosion resistance of duplex stainless steel weldments—A review. *J. Manuf. Process.* **2017**, *25*, 134–152. [CrossRef]
63. Khan, W.N.; Mahajan, S.; Chhibber, R. Investigations on reformed austenite in the microstructure of dissimilar super duplex/pipeline steel weld. *Mater. Lett.* **2021**, *285*, 129109. [CrossRef]
64. Kotechi, D.J.; Siewert, T.A. WRC-1992 Constitution Diagram for Stainless Steel Weld Metals: A sodification of the WRC-1988 Diagram. *Welding* **1992**, *71*, 172.
65. Mercelis, P.; Kruth, J.P. Residual stresses in selective laser sintering and selective laser melting. *Rapid Prototyp. J.* **2006**, *12*, 254–265. [CrossRef]
66. Brown, D.W.; Adams, D.P.; Balogh, L.; Carpenter, J.S.; Clausen, B.; King, G.; Reedlunn, B.; Palmer, T.A.; Maguire, M.C.; Vogel, S.C. In Situ Neutron Diffraction Study of the Influence of Microstructure on the Mechanical Response of Additively Manufactured 304L Stainless Steel. *Metall. Mater. Trans. A* **2017**, *48*, 6055–6069. [CrossRef]
67. Wu, A.S.; Brown, D.W.; Kumar, M.; Gallegos, G.F.; King, W.E. An Experimental Investigation into Additive Manufacturing-Induced Residual Stresses in 316L Stainless Steel. *Metall. Mater. Trans. A* **2014**, *45*, 6260–6270. [CrossRef]
68. Shamsujjoha, M.; Agnew, S.R.; Fitz-Gerald, J.M.; Moore, W.R.; Newman, T.A. High Strength and Ductility of Additively Manufactured 316L Stainless Steel Explained. *Metall. Mater. Trans. A* **2018**, *49*, 3011–3027. [CrossRef]
69. Chen, W.; Voisin, T.; Zhang, Y.; Forien, J.-B.; Spadaccini, C.M.; McDowell, D.L.; Zhu, T.; Wang, Y.M. Microscale residual stresses in additively manufactured stainless steel. *Nat. Commun.* **2019**, *10*, 4338. [CrossRef]
70. Wang, H.; Wang, A.; Li, C.; Yu, X.; Xie, J.; Liu, C. Effect of Secondary-Phase Precipitation on Mechanical Properties and Corrosion Resistance of 00Cr27Ni7Mo5N Hyper-Duplex Stainless Steel during Solution Treatment. *Materials* **2022**, *15*, 7533. [CrossRef] [PubMed]
71. Kurdi, A.; Tabbakh, T.; Basak, A.K. Microstructural and Nanoindentation Investigation on the Laser Powder Bed Fusion Stainless Steel 316L. *Materials* **2023**, *16*, 5933. [CrossRef]